Master Thesis in Geographical Information Science nr 216

Monitoring Landslide Disturbance and Forest Recovery in Afromontane Landscapes: The Case of Nyungwe Forest Reserve, Rwanda

Ingrid Martha Kintu

2026
Department of
Physical Geography and Ecosystem Science
Centre for Geographical Information Systems
Lund University
Sölvegatan 12
S-223 62 Lund
Sweden

Ingrid Martha Kintu (2026). Monitoring Landslide Disturbance and Forest Recovery in Afromontane Landscapes: The Case of Nyungwe Forest Reserve, Rwanda

Master's degree thesis, 30 credits in Master in Geographical Information Science (GIS)

Department of Physical Geography and Ecosystem Science, Lund University

Monitoring Landslide Disturbance and Forest Recovery in Afromontane Landscapes: The Case of Nyungwe Forest Reserve, Rwanda

---

Ingrid Martha Kintu

Master thesis, 30 credits, in Geographical Information Sciences

Supervisor:

Dr. Thomas Pugh

Department of Earth and Environmental Sciences, Lund University

Exam Committee:

Dr. Wenquan Dong

Department of Physical Geography and Ecosystem Science, Lund University

Ms. Calyne Khamila

Department of Physical Geography and Ecosystem Science, Lund University

Acknowledgements

I would like to thank my supervisor, Dr. Thomas Pugh, for his consistent support and insightful feedback throughout this thesis. His guidance has been invaluable at every stage of the research and writing process. I would also like to thank Dr. David Tenenbaum for his guidance and timely support throughout the programme.

My deepest appreciation goes to my family and friends for their patience, motivation, and unwavering support during this journey.

Without all these individuals, this thesis would not have been possible, and I am grateful to them.

Abstract

This study examines landslide occurrence and post-landslide recovery dynamics in Nyungwe Forest Reserve, Rwanda, using a combination of multi-temporal landslide mapping, environmental and geomorphological predictor analysis, and an assessment of the Tropical Moist Forest (TMF) product. A landslide inventory covering the period from 2000 to 2024 was produced using high-resolution optical imagery. This inventory represents the most complete record of landslide activity in Nyungwe so far and captures both the spatial distribution of failures and how their frequency has varied over nearly twenty-five years.

Using Frequency Ratio (FR) and Binary Logistic Regression (BLR), the study found that steep slopes, rainfall, proximity to roads, profile curvature and exposure of slopes to the east are the main factors linked to landslide occurrence within the reserve. Together, the two approaches provided complementary insights: FR highlighted where landslides tend to cluster within specific variable classes, while BLR identified which predictors remain significant when considered simultaneously.

The evaluation of the TMF product showed that it can detect medium-to-large landslides but often misses small, localised failures. This is mainly due to Landsat's 30-meter spatial resolution, temporal rules in the TMF classification system, cloud-related gaps, and spectral confusion. Most disturbance trajectories were still ongoing by 2024, meaning many were right-censored. Only a small number of landslides showed full disturbance-to-regrowth cycles, while others showed partial canopy recovery. Of note are the regrowth patterns in the reserve, with early vegetation return mostly dominated by pioneer tree species and lianas which can alter long-term recovery pathways.

Overall, this study demonstrates the value of combining landslide mapping, statistical modelling, and long-term satellite-derived forest disturbance data to understand forest ecosystems in tropical montane environments. The findings also highlight the limitations of medium-resolution forest monitoring products for detecting small landslides and emphasise the need for future research that incorporates higher-resolution optical and radar data, such as Sentinel-2 and Sentinel-1, to improve detection accuracy and better track post-disturbance recovery.

Table of Contents

List of Tables

List of Figures

List of Abbreviations

BLR	Binary Logistic Regression
FR	Frequency Ratio
GLC	Global Landslide Catalogue
LiDAR	Light Detection and Ranging
LULC	Land Use Land Cover
NASA	National Aeronautics and Space Administration
NDVI	Normalised Difference Vegetation index
OSM	OpenStreetMap
SPI	Stream Power Index
SRTM	Shuttle Radar Topography Mission
TMF	Tropical Moist Forest
VIF	Variance Inflation Factor
WI	Wetness Index

1. Introduction

1.1 Background

Landslides are a major disturbance in tropical montane ecosystems, acting as a primary driver of landscape change and shaping long-term vegetation and habitat dynamics (Freund & Silman, 2023). Their frequency is expected to increase under climate-driven intensification of extreme rainfall, amplifying their ecological impacts in these sensitive environments (Buma & Pawlik, 2021). In Rwanda, landslides represent one of the most significant environmental pressures, contributing to long-term changes to soils, water resources, and biodiversity (Hishamunda et al., 2024). Despite their importance, knowledge gaps remain regarding the environmental and geomorphological factors that influence landslide occurrence and the processes of vegetation recovery that stabilise disturbed slopes. This research seeks to address these gaps by examining the drivers of landslides within Nyungwe Forest Reserve.

Earth observation technologies provide essential tools for monitoring natural disturbances and understanding their ecological impacts (Freund & Silman, 2023). Advances in remote sensing have produced forest-monitoring datasets that offer opportunities to track disturbance and recovery at landscape scales (Hansen et al., 2013; Vancutsem et al., 2021). However, the reliability and practical utility of these products require evaluation. In this study, the Tropical Moist Forest (TMF) product is used to detect landslide-induced forest change and subsequent regrowth in the Afromontane landscape of Nyungwe Forest Reserve, providing a basis for assessing both landslide dynamics and the performance of TMF in capturing post-disturbance recovery.

1.2 Research Questions and Objectives

1.2.1 Research Questions

1. What is the spatial distribution and frequency of landslides within Nyungwe Forest Reserve between 2000 and 2024?
2. What environmental and geomorphological factors most strongly influence landslide occurrence in Nyungwe Forest Reserve between 2000 and 2024?
3. To what extent can the TMF product detect landslide-related forest disturbance at pixel level when compared with the landslide inventory?

4. What patterns of post-landslide forest recovery can be observed using the TMF product?

1.2.2 Research Objectives

1. To compile a multi-temporal landslide inventory for Nyungwe Forest Reserve (2000 to 2024) using high-resolution imagery.
2. To assemble a suite of environmental and geomorphological predictor variables relevant to landslide processes in Afromontane landscapes and determine the relationship between these variables and landslide occurrence.
3. To conduct a pixel-level assessment of the Tropical Moist Forest (TMF) product to evaluate its ability to detect landslide-induced forest disturbance.
4. To examine post-landslide forest recovery patterns using the TMF product.

2. Background - Literature review

2.1 Introduction

This literature review examines the concept and development of landslide inventories, with attention to the methods by which they are constructed and applied. It identifies and evaluates existing inventories relevant to the study area, highlighting their contributions and limitations. The chapter also explores landslides as a disturbance process in tropical montane forests, emphasising their ecological impacts, the factors influencing their occurrence, and the mechanisms of forest recovery that follow such events. Furthermore, it considers the TMF product, as a tool for monitoring disturbance events, analysing forest dynamics, and providing insights into patterns of change.

2.2 Landslides as a Disturbance Factor in Tropical Montane Forests

Landslides are a recurrent natural disturbance in tropical montane forests, leaving enduring physical and ecological imprints on these landscapes (Buma & Pawlik, 2021; Freund & Silman, 2023). There is now clear evidence that global temperatures are rising as a direct result of human greenhouse gas emissions, leading to climate change (Filonchyk et al., 2024; Lee et al., 2024). Landslides are connected to weather and climate patterns, both of which are undergoing transformations that will persist with ongoing anthropogenic climate change. Weather conditions influence landslide activity, with variations in rainfall, such as antecedent moisture, peak rainfall events, cumulative precipitation, seasonal trends, and unstable temperature patterns acting as major triggers. Several studies have shown that local micro-climate conditions intensify these effects to produce increased rates of slope failure in susceptible landscapes (Jakob, 2022; Sharma et al., 2024), and, therefore, add another layer of complexity to the problem caused by climate change because they can influence different types of landslides differently in various locations and time periods. For example, shallow slides and debris flows respond rapidly to precipitation events like heavy rainfalls or rapid snowmelt over relatively short durations, while deep-seated failures respond slowly over longer durations due to changing groundwater and hydrologic regimes (Jakob, 2022). These examples demonstrate how changes in climate interact with geologic systems to create variability in landslide behaviour in different environments.

The study of landslides remains inadequately understood at both the regional and global level, especially when it comes to determining the spatial patterns of landslides and what environmental and geological factors contribute to them (Freund & Silman, 2023; Monsieurs et al., 2018). However, this lack of understanding has been most significant in tropical areas, where there is an elevated potential for landslide susceptibility but the availability of landslide risk assessments remains limited (Monsieurs et al., 2018).

Rwanda's landscape includes steep sloping and mountainous terrains, making Rwanda particularly vulnerable to landslides. These steep slopes, along with rugged topography, provide the potential for large amounts of soil erosion and unstable land surfaces, increasing the possibility of landslide activity (REMA, n.d). In order to better understand how these factors relate to each other within forested environments, there is need to determine how they affect forest ecosystem stability through slope stabilisation and subsequent forest recovery processes important for sustaining the resilience of the natural environment.

2.3 Landslide Inventories

2.3.1 Background

Landslide inventory data is an important resource in landslide studies. Landslide inventories have been utilised as a major source of information, comprising information such as the spatial and temporal characteristics of historic landslides (Huang et al., 2024; Perera et al., 2022). These inventories have become an important tool in landslide hazard mapping, susceptibility modelling, and risk assessment through documentation of the number, size, and locations of previous landslides. Documenting these attributes allows researchers and practitioners to identify factors related to both environmental and anthropogenic conditions which may lead to land sliding and to understand the physical processes that govern failures (Perera et al., 2022).

Landslide inventories are typically classified into two broad categories based on their temporal characteristics, that is to say continuous inventories and event-based inventories (Corominas et al., 2014). Continuous inventories are developed over extended periods, capturing landslide activity across time and offering valuable insights into long-term geomorphological processes and landscape evolution. In contrast, event-based inventories are compiled in the aftermath of specific triggering events such as high intensity rainfall and seismic activity and are designed to record all landslides induced by that single event (Corominas et al., 2014; Huang, Ye, et al., 2022; Oliveira et al., 2024).

For the purposes of this study, a continuous landslide inventory was essential, as the landslide data was integrated with the TMF dataset, a temporal product that provides detailed maps tracking forest dynamics within tropical moist forest regions over time. Given the temporal nature of the TMF dataset, it was imperative that the accompanying landslide inventory also reflected changes over time to allow for meaningful analysis of potential interactions between forest cover dynamics and landslide activity.

Continuous landslide inventories are specifically designed to capture and document landslide occurrences across multiple time periods, thereby offering a more comprehensive understanding of landslide activity. These inventories should include multi-temporal records that detail the timing and location of individual landslide events. Such temporal resolution is vital for assessing patterns and trends in landslide occurrences, particularly in relation to environmental or anthropogenic changes (Corominas et al., 2014). To ensure the reliability and robustness of the assessment, it is critical that the landslide inventory used is as complete and accurate as possible, both spatially and temporally (Xiao & Zhang, 2023).

2.3.2 Existing Landslide Inventories from Literature

To support the research objectives of this study, efforts were made to obtain landslide point data specific to the Nyungwe Forest Reserve in southwestern Rwanda. A literature review was undertaken to identify previous landslide assessments conducted within or near the study area. Through this review, three primary datasets relevant to Rwanda were identified, each offering varying spatial and temporal coverage.

The first and most widely recognised dataset is the landslide inventory for Rwanda available through the National Aeronautics and Space Administration (NASA) Global Landslide Catalogue (GLC), which documents landslide events recorded between 2006 and 2018. This dataset was originally compiled under the Landslide Inventory for the central section of the Western branch of the East African Rift (LIWEAR) project (NASA, 2024), and it provides valuable baseline data on landslide occurrences in the region. However, despite its broad spatial coverage, the GLC has limited resolution and completeness within the Nyungwe Forest Reserve. Notably, no landslides within Nyungwe are recorded in this dataset, highlighting the need for a multi-temporal inventory for this study.

A second relevant dataset was compiled by Depicker et al. (2020) and pertains to the broader Western branch of the East African Rift (WEAR), which extends across much of western Rwanda, notably including the Nyungwe region. This inventory encompasses eastern Democratic Republic of Congo (DRC), Rwanda, and Burundi. Although regional in scope, this dataset provides useful contextual information on landslide activity within the broader rift zone.

In efforts to compile a landslide inventory directly applicable to the specific study area, Depicker et al. (2020) conducted mapping of both shallow and deep-seated landslides within the region through visual interpretation of high-resolution Google Earth imagery spanning 2000 to 2019. This approach, widely accepted in geomorphological studies, has been demonstrated to be effective in identifying landslides (Corominas et al., 2014; Oliveira et al., 2024).

The third dataset identified was generated by Uwihirwe (2021) as part of their research on integrating observed and model-derived groundwater levels in landslide threshold modelling for Rwanda. Uwihirwe (2021) incorporated rainfall-induced landslides sourced from local newspapers, blogs, technical reports, and field observations (Uwihirwe, 2021; Uwihirwe et al., 2022; Uwihirwe et al., 2020). The compilation adhered to standard methodologies and classifications commonly used in landslide research (Kirschbaum et al., 2012; Monsieurs et al., 2018). This dataset adds further depth by linking hydrological conditions with landslide initiation, potentially enhancing the interpretation of causative factors in the Nyungwe region.

Table 2-1 presents a summary of the landslide datasets identified through the literature review, highlighting their spatial extent, temporal coverage and sources.

Table 2-1: Summary details of data identified from literature review

Source	**No. of landslide Points within Rwanda**	**No. of landslide Points within Nyungwe**	**Temporal coverage**
NASA (2024) [1,2]	7	0	2006 to 2018
Depicker et al. (2020)	2587	7	2000 to 2019
Uwihirwe (2021)	71	1	2016 to 2021

[1] Kirschbaum, D. B., Adler, R., Hong, Y., Hill, S., & Lerner-Lam, A. (2010). A global landslide catalog for hazard applications: method, results, and limitations. Natural Hazards, 52(3), 561–575. doi:10.1007/s11069-009-9401-4.

[2] Kirschbaum, D.B., T. Stanley, Y. Zhou (In press, 2015). Spatial and Temporal Analysis of a Global Landslide Catalog. Geomorphology. doi:10.1016/j.geomorph.2015.03.016

In total, eight landslides were identified from the reviewed studies covering the period between 2000 and 2021. However, the limited number of recorded events raised concerns about the completeness of the data within the Nyungwe Forest Reserve. This uncertainty stemmed from the fact that Nyungwe Forest Reserve was not the primary focus of these studies. Given the forested and remote nature of Nyungwe as a protected reserve, it is plausible that landslides occurring deep within the forest interior may go undetected, unreported, and therefore unrecorded in national or global landslide databases. This recognition of potential data gaps underscored the need to specifically target the Nyungwe Forest Reserve for a more detailed landslide inventory, to achieve **Objective 1**.

2.4 Environmental and Geomorphological Factors that Influence Landslide Occurrences

There is no standardised guideline for determining how many variables should be included in susceptibility assessments. Instead, variable selection is typically informed by field observations and evidence from previous research. Predictors such as elevation, slope, planar and profile curvature, aspect, north and east exposure, stream power index (SPI), wetness index (WI), distance to roads and rivers, rainfall, Normalised Difference Vegetation index (NDVI), land-cover and lithology have been identified through the review of landslide literature from Rwanda and other tropical montane environments with comparable geomorphological and climatic conditions. (Depicker et al., 2024; Mind'je et al., 2020; Nsengiyumva et al., 2018).

Elevation influences how gravitational forces act on slopes and is therefore commonly included in landslide susceptibility assessments (Çellek, 2020; Yilmaz et al., 2012). Slope angle, measured in degrees, is one of the controls on slope stability, with steeper gradients generally exhibiting higher failure potential (Abeysiriwardana & Gomes, 2022; Corominas et al., 2014; Mind'je et al., 2020; Sharma et al., 2014). Slope orientation (aspect) can also affect landslide occurrence by shaping patterns of solar radiation, moisture retention, and vegetation cover (Chen et al., 2018; Depicker et al., 2024; Depicker et al., 2020; Yilmaz et al., 2012).

Profile curvature describes the concave or convex form of a slope in the downslope direction and influences water flow acceleration and deceleration. Concave profiles tend to accumulate moisture, increasing saturation and reducing stability, whereas convex profiles promote drainage (Chen et al., 2018; Yilmaz et al., 2012). Plan curvature reflects the curvature of contour lines and affects how water converges or diverges across the slope surface (Wu et al., 2016).

Proximity to rivers can increase landslide susceptibility because channel erosion and concentrated runoff promote saturation and undercutting of adjacent slopes (Chen et al., 2016). WI represents the tendency of water to accumulate in relation to slope, while the SPI estimates the erosive force of flowing water based on contributing catchment area (Conforti et al., 2011; Gholami et al., 2019). Rainfall is widely recognised as a major trigger of landslides in Rwanda, where prolonged or intense precipitation elevates pore-water pressure, reduces soil cohesion, and increases the likelihood of slope failure (Li et al., 2022; Nahayo et al., 2019; Nsengiyumva et al., 2018; Silalahi et al., 2019). Roads can destabilise slopes through excavation, cutting, and alteration of natural drainage pathways. In steep, sensitive terrain such as Nyungwe Forest Reserve, these disturbances can substantially increase landslide susceptibility (Mind'je et al., 2020; Nsengiyumva et al., 2018).

A complementary study was performed during the course of preparing this thesis to evaluate how frequency ratios (FR) and binary logistic regressions (BLR) could be used to determine the environmental and geomorphic variables most significantly correlated with landslide occurrences in Nyungwe Forest Reserve (Kintu, 2025). The study analysed the predictors and found that when FR is utilised in conjunction with BLR, it provides an improved comprehension of landslide behaviour; however, it is the BLR which highlights those variables that exhibit statistical significance toward slope failures, whereas FR identifies the particular classes of these variables that correlate best with the landslide occurrences.

In summary, the literature indicates that numerous environmental and geomorphic variables affect landslide mechanisms. Therefore, there is a necessity for site-specific assessments where variable selection is made based upon relevant theory in analogous environments and based upon demonstrated behaviour within Nyungwe Forest Reserve. Consequently, this emphasises the significance of **Objective Two**, which addressed the compilation of a suitable set of predictors for Nyungwe Forest Reserve and determination of the relationships between them and landslide occurrence using predictive methods such as FR and BLR.

2.5 Remote Sensing Products - Tropical Moist Forest (TMF)

Remote sensing technologies are useful for analysing forest recovery from landslides and provide insight into regrowth patterns under various environmental conditions. Remote sensing has utility for studying large or frequently disturbed areas since it allows researchers to understand variations in forest regeneration at many spatial scales and along many environmental gradients (Freund et al., 2021).

Numerous studies have utilised remote sensing techniques to analyse forest recovery from landslide events utilising advanced tools and methodologies to improve knowledge of ecological succession and regeneration processes. For example, Wang et al. (2024) used change detection methods with Landsat imagery to analyse landslide activity and assess restoration processes in undisturbed landslide zones. This approach provided important insights into temporal trends in recovery and the spatial pattern of regrowth in affected areas. Additionally, Arrogante-Funes et al. (2024) utilised the NDVI as an indicator of vegetation regeneration. They identified the primary drivers of NDVI-based recovery in landslide prone areas using combinations of supervised and unsupervised classification techniques and explainable machine learning models. This methodology enabled the researchers to identify critical environmental and anthropogenic factors controlling regeneration, thus demonstrating the reliability of NDVI as a surrogate for vegetation health following post-disturbances. Freund et al. (2021) utilised Light Detection and Ranging (LiDAR) to examine interactions between environmental variables, topographic characteristics, and forest recovery rates in landslide affected regions.

Although remote sensing technologies have improved substantially for landslide monitoring, the literature review for this thesis indicated a gap in research examining use of the Tropical Moist Forest (TMF) product to identify landslide occurrences and assess forest recovery following landslide events. Developed by the European Commission's Joint Research Centre (JRC), the TMF product is a dataset developed to measure forest cover changes over 42 years in tropical moist forests using Landsat time-series data (European Commission, 2024a, 2024b). This dataset provides essential information about the magnitude and condition of tropical moist forests including documentation of disturbances resulting from deforestation, degradation, natural events, etc., and subsequent forest regrowth. The TMF product's extensive temporal and spatial data present opportunities to investigate forest dynamics in tropical regions allowing researchers to study how natural and anthropogenic disturbances affect ecosystem stability and health throughout time (Vancutsem et al., 2021). Therefore, given that there were no studies investigating if TMF can detect landslide related disturbance and subsequently assess recovery, this research investigates the feasibility of TMF for this purpose, thereby filling the gap identified and meeting **Objective Three**.

2.6 Mechanisms of Slope Stabilisation and Forest Recovery

Tropical montane forests are subject to landslides, which represent one of several forms of natural disturbances occurring in these landscapes world-wide (Dislich & Huth, 2012). Ecosystems globally are experiencing dramatic changes due to increased environmental pressure, especially in developing countries (Delgado Isasi & Marín Briano, 2020). Mountainous regions are being influenced by landslides affecting both the distribution and succession of flora and possibly fauna (Chen et al., 2022).

In addition to directly modifying landscape features immediately surrounding landslide locations, landslides also impart lasting influences on both terrain and ecosystems (Freund & Silman, 2023). Landslides influence ecosystem processes by removing vegetation and the upper soil layers, clearing spaces that facilitate primary succession and allowing new growth to take place under altered environmental conditions. (Crausbay & Martin, 2016; Dislich & Huth, 2012). The interrelations between forest structure and disturbances such as landslides can create emergent properties that influence ecosystem attributes. These include post-disturbance legacies that influence forest structural diversity, species composition and the capacity of the forest to maintain or recover its structure in response to subsequent disturbances (Mitchell et al., 2023).

Forest vegetation enhances hillslope stability by establishing long, deep roots that extend across and penetrate potential failure planes (Buma & Pawlik, 2021). Tree roots are also widely acknowledged for their ability to enhance slope stability by significantly strengthening the soil structure (Cohen & Schwarz, 2017; Crausbay & Martin, 2016; Liu et al., 2021). Through a network of roots that penetrate and bind the soil, trees contribute mechanical support that resists erosion and helps prevent landslides. These roots interlock with soil particles, creating a reinforcing framework that increases soil cohesion and reduces the likelihood of slippage on hillslopes. Over time, this natural reinforcement process is integral to maintaining stable landscapes, particularly in regions susceptible to slope failure (Cohen & Schwarz, 2017; Liu et al., 2021). By aiding in soil recovery and structural resilience, vegetation regeneration plays an integral role in long-term slope stability and ecosystem recovery following a landslide disturbance (Law et al., 2024).

While the role of forests in preventing landslides is well-documented, much less is known about the ecological processes that follow landslide events, especially in regions where landslides occur infrequently yet have profound ecological impacts (Buma & Pawlik, 2021). Studies have been conducted in the Andes including Freund et al. (2021) who conducted an analysis of landslides in the Tropical Andes biodiversity hotspot, leveraging remote sensing techniques such as Lidar to examine how factors such as landslide characteristics, biophysical properties, residual vegetation, and topographic conditions influence canopy height and heterogeneity during forest regeneration. Their findings underscored the critical role of landslide age and elevation as primary drivers of forest recovery. Residual vegetation was identified as a key contributor to hastening regeneration, acting as a foundation for ecological succession. Freund and Silman (2023) further explored the complex ecological roles of landslides in the Andes. Their research revealed variation in plant succession across altitudes, noting distinct species compositions in landslides at low versus high elevations. They also emphasised the role of landslides as natural corridors for tree migration, facilitating species dispersal in response to environmental pressures. Additionally, their work investigated the duration required for full forest recovery and advocated for the use of remote sensing technologies to monitor species composition and ecological dynamics during regeneration.

In Boulder County, Colorado, Buma and Pawlik (2021) examined post-landslide soil and vegetation recovery. Their study highlighted the challenges of regeneration in initiation zones, which were characterised by shallow soils and lower nitrogen content. These areas showed limited vegetation recovery, a problem exacerbated by the warming climate, which further slowed the progression of ecological succession. Dislich and Huth (2012) modelled the long-term effects of landslides on tropical montane forests in Reserva Biológica San Francisco, Ecuador. Their findings indicated that locally, it takes at least 200 years for a post-landslide forest to develop a structure comparable to a mature forest. Landslides reduced forest productivity and created distinct spatial and temporal patterns of tree biomass distribution. On a larger landscape scale, landslides caused significant reductions in overall tree biomass, increased heterogeneity, and established "hotspots" of biomass loss alongside "blind spots" of reduced productivity. These findings underscore the complexity of landslide impacts on tropical forests and the protracted timescales required for recovery.

Forest recovery following landslides in Rwanda and particularly in Nyungwe Forest Reserve remains insufficiently studied. A review of the literature did not identify studies addressing post-landslide ecological recovery in Rwanda and more specifically in Nyungwe Forest Reserve. Most existing work concentrates on landslide susceptibility or hazard mapping rather than post-disturbance forest dynamics. Although studies from other tropical montane forests in the Albertine Rift and beyond (e.g., South America) offer useful conceptual insights, their applicability to Nyungwe Forest Reserve is constrained by differences in geology, rainfall regimes, species composition, and disturbance histories. This gap in knowledge restricts the ability to understand the broader ecological implications of landslides in the reserve. Addressing these gaps is particularly critical for biodiversity-rich areas like Nyungwe Forest Reserve (to be achieved by **Objective 4**), where landslides not only disrupt local ecosystems but also influence regional ecological networks. Understanding the interplay of ecological, topographic, and environmental factors in post-landslide recovery is essential for informing sustainable management and conservation strategies.

3. Methodology

3.1 Study Area

The research was conducted in Nyungwe Forest Reserve, located in southwestern Rwanda (See **Figure 3-1**). This protected area extends between the coordinates 727343 E to 771810 E and 9750920 N to 9686122 N, with altitudes varying from 1,600 to 2,950 meters above sea level. The reserve has extensive forested areas that are interspersed with two significant swamps (Van der Heyden, 2016).

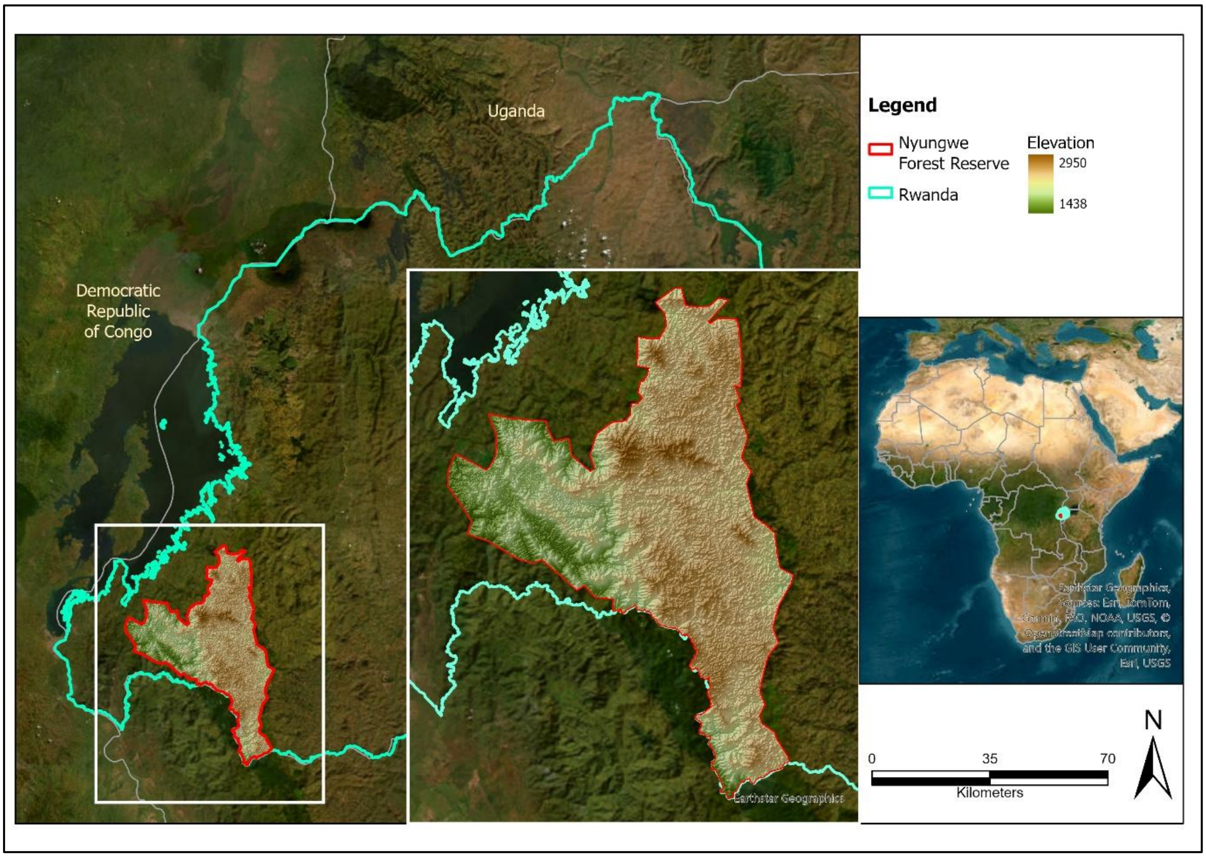

Figure 3-1: Map of the study area

The reserve is comprised of complex topography with steep slopes which make it susceptible to landslides (Mlotha, 2018). Spanning roughly 1,000 square kilometres, Nyungwe stands as the most extensive conservation area in the country (Senyanzobe et al., 2020). This tropical montane rainforest, first recognised as a forest reserve in 1933, connects with Kibira National Park in neighbouring Burundi, forming a critical ecological corridor. Nyungwe serves as an essential conservation stronghold, supporting a diverse range of wildlife that includes numerous mammal and bird species, alongside an extensive variety of tree species (Akayezu et al., 2022). The reserve hosts an array of ecosystems, comprising dense rainforest habitats, scattered savannah patches, and swamp regions. This diversity adds to its ecological richness and underscores its significance as a vital biodiversity hotspot (Udahogora et al., 2024).

3.2 Data

A range of datasets was assembled to address the four research questions and objectives, covering landslide occurrence, environmental and geomorphological predictors, and forest disturbance and recovery. **Table 3-1** provides an overview of each dataset, its purpose within the study, and its source. **Figure 3-2** presents the methodological workflow used in this study. The workflow includes landslide inventory development, extraction and analysis of the influence of the environmental and geomorphological predictors, TMF-based disturbance detection, and assessment of post-landslide forest recovery.

Table 3-1: Datasets used for this research

Research Questions/ Objectives	Data required	Description and Purpose	Source
1	Landslide inventory	Primary dataset used to map landslide occurrences across the study area. Includes the author's manually compiled inventory from Google Earth imagery.	Author's inventory using Google Earth imagery.
2	Elevation, slope, planar and profile curvature, aspect, north and east exposure, stream power index (SPI) and wetness index (WI)	Environmental and geomorphological predictors used to analyse factors influencing landslide occurrence.	NASA Shuttle Radar Topography Mission (SRTM) data (USGS, 2018)
	Distance to roads and rivers	Predictor variables representing anthropogenic and hydrological influence.	OpenStreetMap (OSM) data downloaded via QGIS OSM plugin (QGIS, n.d).
	Rainfall	Climatic predictor used to assess rainfall–landslide relationships.	CHIRPS rainfall data (Climate Hazard Center, 2025)

Research Questions/ Objectives	Data required	Description and Purpose	Source
3 and 4	Tropical Moist Forest (TMF) Product	Primary dataset used to detect forest disturbance associated with landslides and to assess post-landslide forest recovery. Provides annual disturbance and regrowth information for tropical forests.	European Commission Tropical Forest Monitoring Platform (European Commission, 2024a, 2024b).

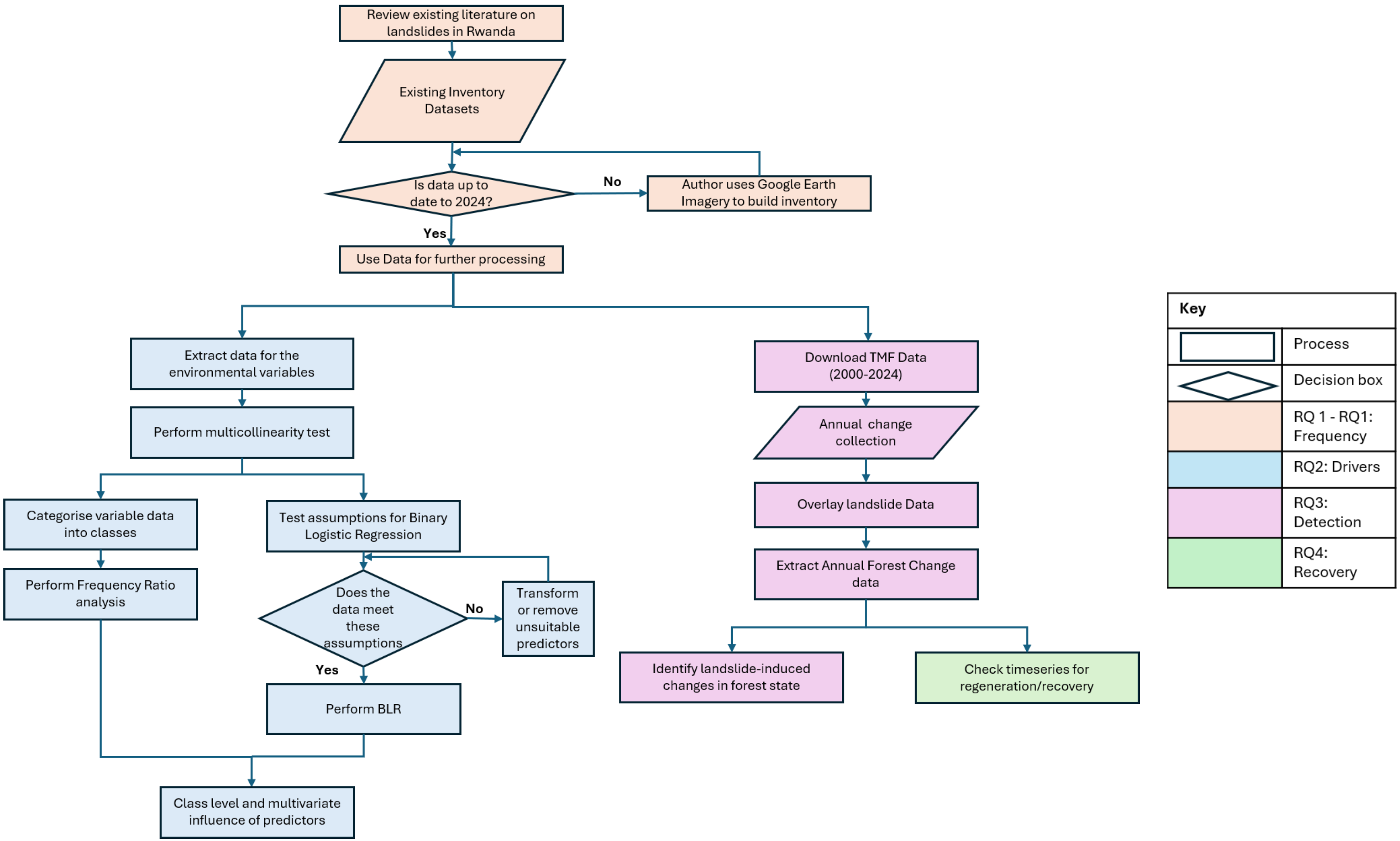

Figure 3-2: Research methodology

3.3 Landslide Inventory Compilation

3.3.1 Landslide Identification process

A compilation of the existing landslide data was done by bringing together two inventories including that compiled by Uwihirwe et al. (2022) and Depicker et al. (2020). Since the inventories were developed for different projects and purposes, rather than specifically for identifying landslides within the Nyungwe Forest Reserve, it was necessary to verify that landslides local to the reserve were included.

A systematic visual inspection of high-resolution Google Earth imagery was undertaken within the boundaries of the reserve. The approach followed the methodology outlined by Depicker et al. (2020), who conducted a visual interpretation of Google Earth imagery across the western branch of the East African Rift. Their work relied on cloud-free satellite images and identified landslides based on their spectral signatures and the distinctive morphological alterations they produce in the landscape. The use of tools such as Google Earth enables landslide identification in remote and sometimes inaccessible terrain such as Nyungwe Forest Reserve (Corominas et al., 2014). Google Earth provides high-resolution satellite imagery together with a timeline tool that enables the examination of land-surface changes across multiple years, an essential capability for detecting past landslide events. This temporal functionality allows sub-annual and multi-year inspection of specific areas, supporting the identification of landslides through observable shifts in vegetation cover, surface texture, and coloration between successive image timestamps. This temporal comparison allows for the estimation of an approximate time of slope failure.

To ensure systematic and complete coverage of the entire reserve, the study area was subdivided into ten manageable sections. All sections were examined sequentially across all available image dates using the timeline tool, so that no area of the reserve was missed and that all landslide events with visible imagery from 2000 to 2024 were identified. A review of all time-stamped images for each section was conducted and classified as being either usable (clear, cloud-free and capable of landslide detection) or non-usable (partially or completely cloud-covered, obscured or missing). The classification results were subsequently aggregated to provide an annual assessment of usable imagery availability for the entire reserve. Documentation of usable imagery availability is crucial in assessing how well the temporally distributed mapped landslide information represents landslide activity throughout the reserve. An absence of usable imagery in a given year does not imply the lack of landslide activity in that year but indicates the period when the detection of landslide activity was impossible. Therefore, this record enabled an evaluation of the completeness of the inventory in the context of the reserve. Each landslide was identified by unique morphologic characteristics indicative of landslide movement, including scarp formation, exposure of soil relative to surrounding vegetation, deposition at the base of the slope, and long linear disturbances oriented parallel to the slope. For each landslide, a set of attributes was collected. Each landslide includes a point location representing the position of the scarp and the earliest date that the feature appears in the Google Earth Timeline. Due to the nature of the Google Earth system, which captures imagery at discrete points in time versus continuously capturing it, the first observed year of landslide occurrence was recorded, rather than the exact day upon which failure occurred. For each landslide, both point-based representations (i.e., scar location) and polygonal representations (e.g., extent of each landslide scar) were obtained.

3.3.1.1 Google Earth Image Interpretation

In interpreting imagery, several morphological and surface features were considered to confirm the presence of landslides. These include visible scarps along with areas of bare earth or exposed soil, which often appear as sharp colour contrasts against the surrounding vegetated landscape (see **Figure 3-3**). At the downslope end, depositional features are further indicators. The overall shape of the disturbed area is also an important cue with landslides tending to form elongated patches aligned with the slope gradient, characterised by abrupt boundaries, where forest cover transitions suddenly into disrupted terrain.

Figure 3-3: (a) Landslide scarp (b) Landslide alongside road (c) Before (2020) and after (2021) landslide occurrence with deposition material in the road (d) Anthropogenic land clearance in the reserve

During the inspection, numerous landslide features were observed, including along roads, where the slope-cutting associated with road construction likely contributes to instability (Mind'je et al., 2020; Nsengiyumva et al., 2018). In some cases, boulders installed as mitigation structures were visible (see **Figure 3-3b**), and signs of accumulated debris on the road surface provided confirmation of recent or recurring landslide activity (see **Figure 3-3c**).

Given the occurrence of anthropogenic activities within the reserve (Kayiranga et al., 2016; Udahogora et al., 2024), it was essential to distinguish between natural landslides and anthropogenic activities. Several criteria were applied in this differentiation. Shape and pattern served as key indicators. Forest clearance typically results in regular, geometric features while landslides appear irregular (Huang et al., 2024; Huang, Yan, et al., 2022; L. Li et al., 2022). Location and context also play a crucial role in classification. Areas of forest clearance are usually situated near roads, tracks, or settlements, and often show visible signs of human activity, such as parked vehicles (see **Figure 3-3d**). This overall process of landslide identification resulted in a landslide inventory database for the Nyungwe Forest Reserve.

3.4 Influence of environmental and geomorphological factors on landslide occurrences in Nyungwe Forest Reserve

3.4.1 Multicollinearity

Multicollinearity reduces the reliability of landslide susceptibility models because highly correlated predictors make it difficult for the models to separate their individual effects, producing unstable coefficients and limiting how confidently each variable's role can be interpreted. Testing for multicollinearity therefore helps ensure that only independent predictors are retained, strengthening both model stability and overall performance (Mind'je et al., 2020). In this research, the variance inflation factor (VIF) was used to assess the presence of multicollinearity among the predictor variables. Values above 2 are commonly interpreted as indicating problematic levels of shared variance (Mind'je et al., 2020; Sujatha & Sridhar, 2021). All variables recorded VIF values below 2, indicating that multicollinearity was not a concern. As a result, no variables were removed during this stage, and all predictors were retained for subsequent analysis.

3.4.2 Models

3.4.2.1 Frequency Ratio (FR)

The FR model is a bivariate statistical approach that assesses the degree of association between landslide occurrence and individual predictor variables. It operates by comparing the proportion of landslides within a given class of a variable to the proportion of that class within the entire study area (Sharma et al., 2014; Silalahi et al., 2019). **Equation (1)**.

$$\mathrm{FR} = \frac{\frac{N_{si}}{N_S}}{\frac{N_i}{N}} \qquad \textbf{(1)}$$

Where:

N_{si} = Number of landslide pixels in class

N_s = Total number of landslide pixels in the study area

N_i = Total number of pixels in class i (both landslide and non-landslide)

N = Total number of pixels in the study area

The independent treatment of each conditioning factor in the FR approach allowed the method to highlight how classes in specific environmental variables correspond with landslide occurrence.

Data preparation for FR Model

To prepare the predictor variables for the FR analysis, each variable was reclassified into discrete classes. **Table 3-2** provides a summary of all variables and their classifications used in the FR model.

Table 3-2: Data preparation for FR analysis

Variable	Classes
Elevation	
	1700 – 2000
	2000 – 2300
	2300 – 2600
	2600 – 3000
Aspect	
	Flat -1
	North (N) 0 - 22.5 and 337.5 - 360
	Northeast (NE) 22.5 - 67.5
	East (E) 67.5 - 112.5
	Southeast (SE) 112.5 - 157.5
	South (S) 157.5 - 202.5
	Southwest (SW) 202.5 - 247.5
	West (W) 247.5 - 295.5
	Northwest (NW) 295.5 - 337.5
WI	
	2.5 - 5
	5 - 7.5
	7.5 - 10
	10 - 12.5
	>12.5
SPI	
	<0.22
	0.22 – 0.5
	0.5 - 3
Slope	
	0 – 5
	5 – 15
	15 – 25
	25 – 35
	35 – 63

Variable	Classes
Rainfall	
	1300 - 1450
	1450 - 1600
	1600 - 1750
Broad North Exposure	
	Other Direction
	Broad North Facing
East Exposure	
	Other Direction
	East Facing
Profile Curvature	
	-2 - -0.005
	-0.005 - 0.005
	0.005 - 5
Plan Curvature	
	-11 - -0.01
	-0.01 - 0.01
	0.01 - 11
Distance to Roads	
	0 - 100
	100 - 200
	200 - 300
	300 - 400
	400 - 500
	>500
Distance to Rivers	
	0 - 100
	100 - 200
	200 - 300
	300 - 400
	400 - 500
	>500

3.4.2.2 Binary Logistic Regression (BLR)

BLR is a multivariate statistical model that estimates the probability of landslide occurrence as a function of multiple predictor variables simultaneously (Abeysiriwardana & Gomes, 2022). BLR removes the least significant variable one at a time, refits the model after each removal, and stops when all remaining variables are statistically significant. BLR is based on **Equation (2)** (Sujatha & Sridhar, 2021).

$$p = \frac{e^z}{1+e^z} = \frac{1}{1+ e^{-z}} \tag{2}$$

In BLR, p represents the probability of a landslide occurring, with values ranging between 0 and 1. The term z can take any value from negative to positive infinity and is calculated as a linear combination of the independent variables, as shown in Equation **(3)**. In this expression, $\boldsymbol{b_0}$ is the intercept of the model while $\boldsymbol{b_i}\ (\boldsymbol{i} = \boldsymbol{1, 2, \ldots\ldots, n})$ are the coefficients generated by the regression analysis for each independent variable. The number of independent variables is denoted by n and $\boldsymbol{X_i}$ (i = 1, 2, ……, n) represents each of these variables. In this study, variables with a significance level of $p < 0.05$ were considered to have a statistically significant influence.

$$\boldsymbol{z = b_0 + b_1X_1 + b_2X_2 + b_3X_3 + \cdots + b_nX_n} \quad \textbf{(3)}$$

BLR does not require continuous predictors to follow a normal distribution because the model is estimated using maximum likelihood rather than least squares (Hosmer et al., 2013). BLR relies on several key assumptions such as the predictors should not exhibit strong inter-correlations, observations must be independent of one another, and any continuous variables included in the model are expected to show a linear relationship with the logit transformation of the dependent variable (Abeysiriwardana & Gomes, 2022; García-Rodríguez et al., 2008; IBM, 2024). Tests to ensure that these assumptions were met were carried out before performing BLR. Additionally, all continuous predictors were converted to z-scores prior to model fitting. This ensured that variables measured in different units were comparable and helped avoid scaling issues.

3.5 Detection rate of the TMF product for landslides

3.5.1 Confusion Matrix

The confusion matrix, or error matrix, is a widely adopted accuracy assessment method that provides a standardised method to evaluate performance by accounting for errors of omission and commission (Ariza-López et al., 2018; Barsi et al., 2018; Foody, 2005; Foody, 2002). In this study, it was used to quantify how reliably the TMF product detected forest changes associated with mapped landslides. The evaluation dataset contained two categorical attributes: a reference column indicating landslide presence based on the inventory, and a column indicating whether the TMF product registered a corresponding change. These paired observations formed the basis for constructing the confusion matrix.

Data preparation for confusion matrix

To assess the TMF product's ability to detect landslide-induced forest disturbance, the landslide inventory was compared with the annual TMF dataset at the pixel level. This involved overlaying the spatial extent of each mapped landslide onto the TMF annual layers and examining whether the product recorded a change in forest condition during the year of the landslide event.

For each landslide-affected pixel, the TMF product was inspected to determine whether it showed a transition from an undisturbed forest class (e.g., tropical moist forest) to a degraded class indicative of disturbance or from degraded to a deforested class. Pixels that showed such a transition were recorded as detected changes, while those that did not were classified as missed detections. These outcomes allowed each pixel to be categorised as a true positive (correctly detected change) or a false negative (undetected change), forming the essential components of the confusion matrix used to quantify detection accuracy (Barsi et al., 2018; Foody, 2002).

3.5.2 Influence of Landslide Area on TMF Detection

Landslide polygons from the mapped inventory were attributed with a binary TMF detection variable (TMF_Coded = 1 for detected, 0 for not detected). Polygon areas were calculated in square metres using the geometry of each mapped landslide. The final dataset comprised 107 landslides with area and detection information. Landslide areas ranged from 62 m^2 to 14,532 m^2, producing a skewed distribution. To ensure meaningful comparison between detected and undetected events, histograms of area for detected and undetected landslides were generated.

3.5.3 Pixel-level TMF detection of landslide-related forest disturbance

In the TMF annual change maps, areas classified as degraded tropical moist forests are represented by pixels that experienced up to three short-term disturbances within the period from 1990 to 2024. Each of these disturbances is characterised by a temporary loss of tree cover in a Landsat pixel, lasting no longer than 900 days. Importantly, for a disturbance to be categorised as degradation, it must be followed by a recovery period of at least two consecutive years during which no additional disturbance is detected (European Commission, 2024b). This captures processes such as small-scale clearing, or natural events that temporarily affect forest cover without leading to its complete conversion.

Deforestation, by contrast, involves the conversion of undisturbed or degraded tropical moist forest into another type of land cover, such as agriculture, infrastructure, or barren land. Within the TMF framework, deforestation is identified as a long-term disturbance persisting for more than 900 days, reflecting a shift from temporary canopy loss to a sustained absence of forest cover. The year of deforestation is assigned either to the onset of this prolonged disturbance or, in cases where multiple short-term disturbances occur consecutively, to the start of the very first disturbance if three or more are recorded in sequence (European Commission, 2024b). This approach ensures that both gradual and abrupt forest clearances are consistently captured, providing a picture of forest dynamics over time. In this study, landslide detection by TMF was defined as the transition from undisturbed forest (class 1) to degraded (class 2) or deforested forest (class 3), or from degraded forest (class 2) to deforested forest (class 3).

3.6 Post-Landslide Vegetation Recovery Using the TMF Product

The TMF product defines regrowth as a two-stage transition in which a pixel first shifts from intact forest to deforested land and later from deforested land to regrown forest. A minimum of three consecutive years of stable forest cover is required before a pixel is classified as regrowth, ensuring that detected recovery represents genuine forest regeneration rather than short-term vegetation fluctuations (Vancutsem et al., 2021). Mapped landslide locations were overlaid onto the annual TMF layers to identify potential recovery within landslide footprints. For each landslide, the TMF time series were examined from the year of the event onward to determine whether a transition to regrowth occurred in subsequent years. This pixel-level assessment made it possible to identify landslides for which the TMF product detected both disturbance and recovery. Interpretation of TMF-identified regrowth drew on environmental and ecological characteristics of Nyungwe Forest Reserve as well as data-related considerations such as classification thresholds and spatial- temporal resolution. Together, these evaluations provided an overall indication of the TMF product's ability to detect landslide-induced forest change and subsequent vegetation recovery.

3.7 Ethical considerations

Ethical considerations were integrated throughout the research process and were upheld during data collection, analysis, and presentation of results, as emphasised by Creswell (2009). Since this is a quantitative study that does not involve questionnaires, surveys, or direct field data collection, no ethical concerns related to human interaction occurred. The research relied solely on geospatial and remote sensing datasets obtained from online sources. To ensure ethical integrity, transparency has been maintained in both the methodology and data sources. All data providers have been appropriately credited, with adherence to data-sharing agreements and intellectual property rights.

4. Results and Discussion

4.1 Introduction

This chapter presents the outcomes of the analyses undertaken for Nyungwe Forest Reserve. The results are organised to reflect the sequential workflow of the study, beginning with the identification and mapping of landslides from Google Earth imagery, followed by an assessment of imagery availability across the study period. This establishes the inventory, which in turn underpins the subsequent statistical and spatial analyses. The chapter then reports the outcomes of the FR analysis, the BLR modelling, and the TMF assessment.

4.2 Landslide Inventory

From the landslide identification process, **107** landslide locations from 2000 to 2024 (see **Figure 4-1**) were mapped.

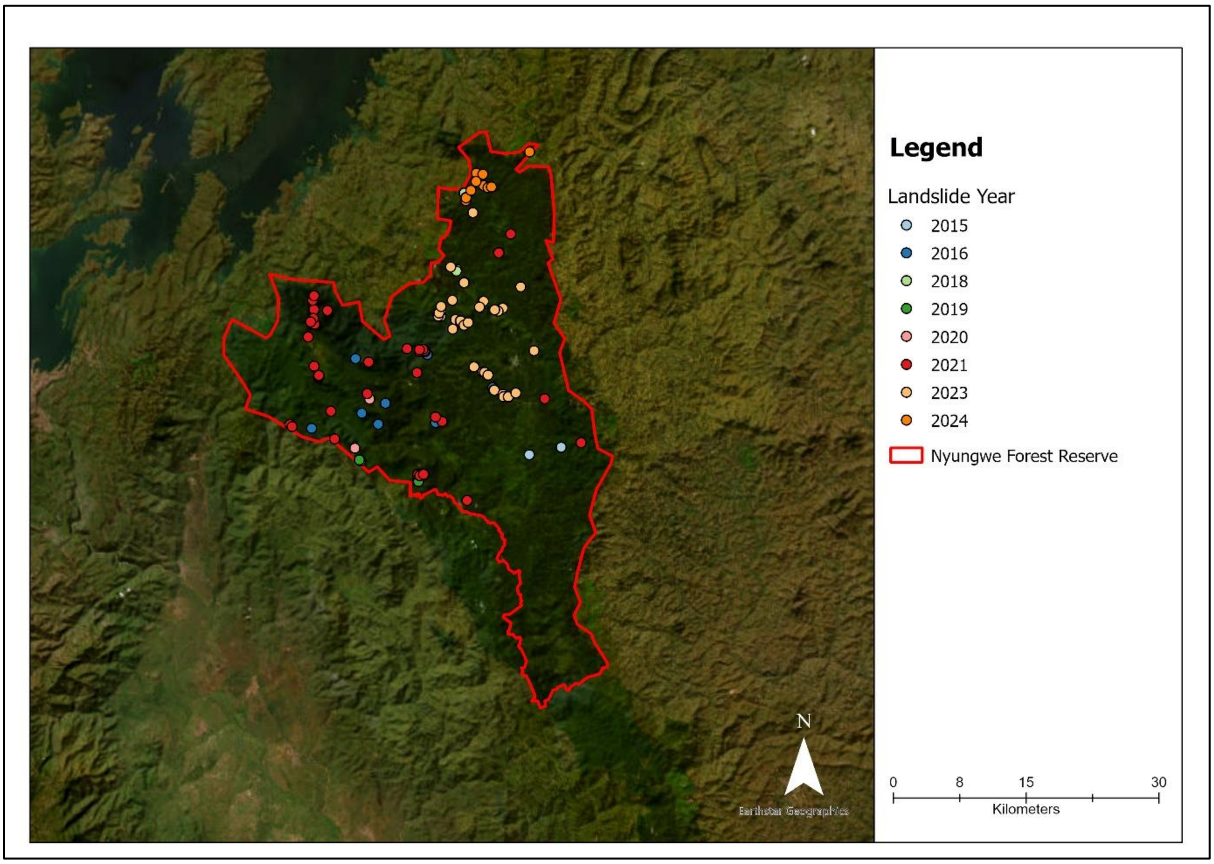

Figure 4-1: Map of landslides identified within Nyungwe Forest Reserve

The assessment of imagery availability revealed substantial temporal variability in the Google Earth archive for Nyungwe Forest Reserve. Usable imagery was present in only 10 of the 24 years between 2000 and 2024, representing ~42% coverage of the study period. Importantly, even this coverage was not uniform across the reserve. Because Google Earth imagery is mosaiced, individual years may include high-quality scenes for some parts of the reserve while other areas remain unmapped or represented by lower-quality tiles. Similar limitations in spatial completeness and temporal consistency have been documented in other studies using Google Earth for landslide mapping (Rabby & Li, 2019; Sukristiyanti et al., 2021). In Nyungwe forest reserve, periods, particularly 2000 to 2004, 2008 to 2014 and 2017, had no imagery in any section, whereas years such as 2005 - 2007, 2015, 2020, 2023 and 2024 offered only partial coverage. In contrast, years including 2016, 2018, 2019, 2021, and 2022 had imagery across most sections, enabling more reliable landslide detection within these years. A full schedule of image availability is available in **Appendix A**.

The highest number of landslides in the inventory were recorded in 2021 and 2023 (see **Table 4-1**). It should be noted that landslides may have occurred within the study area during other years; however, they were not identifiable due to image availability for those specific years. This is due to the date of imagery acquisition not coinciding with the timing of the landslide event itself, such that some failures may only become visible, or remain invisible, depending on when suitable imagery was captured (Sukristiyanti et al., 2021).

The availability and quality of usable imagery were the two main factors influencing landslide identification. In some years, Google Earth provided no interpretable imagery, while in others, persistent cloud cover obscured the land surface and prevented clear delineation of landslide scars. Cloud cover is a well-known source of incompleteness in landslide inventories (Guzzetti et al., 2012; Peng et al., 2021), and its impact is particularly pronounced in Rwanda, where cloudiness is frequent and often dense throughout the year. This makes mapping landslide features challenging (Ruusa et al., 2022). Similar challenges have been reported elsewhere; for example, Depicker et al. (2020) relied exclusively on cloud-free scenes when compiling their inventory. The problem is therefore amplified in tropical regions, where persistent cloud cover is a characteristic environmental constraint. Due to these limitations, the number of landslides identified reflects both actual events and the availability of usable imagery. As a result, the temporal pattern represents detectability, not true annual landslide frequency.

Table 4-1: Image Availability and Number of landslides Identified by Year

Year	Image Availability	Number of Landslides
2000 - 2004	-	-

Year	Image Availability	Number of Landslides
2005 - 2007	Present	-
2008 - 2014	-	-
2015	Present	2
2016	Present	13
2017	-	-
2018	Present	4
2019	Present	6
2020	Present	3
2021	Present	33
2022	Present	1
2023	Present	34
2024	Present	11

In addition to having access to clear imagery, landslide detectability through Google Earth also relies on how long landslide scars remain visible before being obscured by vegetation regrowth. Rapid post-landslide revegetation is widely recognised as a major obstacle to identifying landslide scars in tropical forest environments when imagery is not captured soon after the event (Samodra et al., 2017). Similar challenges have been documented by Sukristiyanti et al. (2021) in Indonesia, where dense vegetation regrowth rapidly obscures surface disturbance, leading to under-representation of older landslides in inventories derived from optical imagery. The patterns observed in Nyungwe Forest Reserve align with this broader evidence. Analysis of landslides with consecutive years of usable imagery indicates that scars remain clearly distinguishable for approximately three to five years before blending into the surrounding canopy. Beyond this period, progressive vegetation recovery obscures scar boundaries, substantially reducing the likelihood of detection in later imagery (see **Figure 4-2**). This visibility window is consistent with the rapid recovery dynamics reported across other tropical forest systems and highlights the inherent limitations of reconstructing long-term landslide activity using Google Earth imagery.

Figure 4-2: Scar visibility window at a landslide location within Nyungwe Forest Reserve

This visibility window has important implications for interpreting the completeness of the landslide inventory. In years where imagery gaps were short (e.g., a single missing year), most landslides were still detectable in subsequent images because scars persisted long enough to be captured once imagery became available again. However, extended periods without usable imagery, such as 2000 to 2004 and 2008 to 2014, likely resulted in missed events, especially smaller or shallow landslides that revegetate more rapidly. Based on the typical annual landslide rate derived from years with usable imagery (approximately 5 - 6 events per year), and assuming that these years provide a representative baseline for the full study period, an estimated 74 landslides were likely missed during the 13 years in which no interpretable imagery was available. This estimate excludes outlier years (2021 and 2023) with unusually high landslide counts and assumes relatively stable landslide activity over time (see **Appendix B**). Understanding vegetation recovery dynamics therefore provides essential context for evaluating the reliability of the mapped temporal pattern and the potential under-representation of landslides during periods of limited imagery coverage (Samodra et al., 2017; Sukristiyanti et al., 2021).

Another factor that influenced the process was the subjective nature of visual interpretation. To address this, clear and consistent criteria such as the shape of the scar, the sharpness of its edges, and its location on the slope were applied. Even with these measures, some uncertainty remained, particularly when distinguishing between natural slope failures and human activities like forest clearance. For this reason, the interpretation required attention and the application of informed judgment based on repeated observation and comparison across different images.

4.3 Environmental and Geomorphological Drivers of Landslide Occurrence

4.3.1 Multicollinearity

The test for multicollinearity found that all 12 variables had VIF values below 2 (**Table 4-2**). Among them, the wetness index showed the highest VIF at 1.967, while distance to rivers had the lowest at 1.112. As all variables satisfied the required threshold, each was retained for subsequent analyses. VIF values below 2 indicate that the predictors are not strongly correlated, meaning each variable contributes unique information to the model rather than duplicating the effect of another predictor (Mind'je et al., 2020; Sujatha & Sridhar, 2021).

Table 4-2: VIF for the predictor variables

Variables	VIF
East Exposure	1.430
Aspect	1.215
North Exposure	1.440
Elevation	1.194
Profile Curvature	1.245
Plan Curvature	1.264
Rainfall	1.257
Wetness Index	1.967
Slope	1.419
Stream Power Index	1.259
Distance to Roads	1.225
Distance to Rivers	1.112

4.3.2 Frequency Ratio (FR)

Table 4-3 summarises the FR results, with the highest values per class highlighted. Elevation showed its strongest association with landslides in the 2600 - 3000 m (FR = 2.790) and 2300 - 2600 m (FR = 0.973) ranges, while lower elevations displayed weaker relationships. This pattern is consistent with studies noting that higher altitudes are prone to gravitational stresses and hence landslides (Cellek, 2021; Yilmaz et al., 2012). Slope gradient followed the expected trend reported widely in the literature (Abeysiriwardana & Gomes, 2022; Corominas et al., 2014), with very steep slopes (35 - 63°) showing the highest susceptibility (FR = 2.977). Gentle slopes (0–5°) were more stable, reflecting the well-established role of slope angle as a primary control on stability. Aspect results revealed that south-facing slopes were most prone to landslides (FR = 1.738), with southwest and southeast aspects also showing elevated values, followed closely by the east-facing slopes. For both east and north exposure, landslides were found to be more common in other aggregated direction. The influence of aspect on landslide occurrence is well documented, as slope orientation shapes microclimatic conditions, solar radiation, and moisture retention, which can affect slope stability (Chen et al., 2018; Depicker et al., 2024; Depicker et al., 2020; Yilmaz et al., 2012).

Curvature variables further emphasised the role of hydrological concentration. Concave profile curvature had the highest FR (1.334), consistent with evidence that concave slopes accumulate water and promote saturation (Chen et al., 2018; Yilmaz et al., 2012). Plan curvature showed a similar pattern, with concave areas recording the highest FR (1.206), indicating that convergence zones enhance instability (Wu et al., 2016).

Hydrological indices also showed meaningful relationships. Higher WI classes (10–12.5) had elevated FR values (1.210), and SPI peaked in the 0.5–3 range (FR = 1.841), reflecting the influence of water accumulation and erosive power on slope failure area (Conforti et al., 2011; Gholami et al., 2019). However, rainfall displayed an unexpected pattern: the intermediate rainfall class (1450–1600 mm) had the highest FR (1.524), while the wettest areas (1600–1750 mm) had the lowest (0.425). This contrasts with the commonly reported role of rainfall as a dominant trigger for landslides (Li et al., 2022; Nahayo et al., 2019; Nsengiyumva et al., 2018; Silalahi et al., 2019), suggesting that in Nyungwe, rainfall interacts with other stabilising terrain conditions.

Proximity to infrastructure emerged as a strong predictor. Areas within 100 m of roads had an exceptionally high FR (7.770), reflecting the destabilising effects of road cuts and drainage disruption in steep terrain (Mind'je et al., 2020; Nsengiyumva et al., 2018). Similarly, areas within 100 m of rivers showed elevated susceptibility (FR = 1.682), consistent with the role of fluvial undercutting and saturation near channels (Chen et al., 2016).

Table 4-3: Landslide predicting variables and their frequency ratios, showing how strongly each class is associated with landslide occurrence relative to the overall study area

Variable	Classes	No. of Landslide Pixels in Class	Total No. of Pixels in Class	Landslides Pixels (%)	Domain Pixels (%)	FR
Elevation	1700 – 2000	282	1813581	15.186	16.153	0.940
	2000 – 2300	298	2282661	16.047	20.331	0.789
	2300 – 2600	1079	6702057	58.104	59.694	0.973
	2600 – 3000	198	429057	10.662	3.822	2.790
Aspect	Flat -1		594	0.000	0.005	0.000
	North (N) 0 - 22.5 and 337.5 - 360	195	1541619	10.501	13.589	0.773
	Northeast (NE) 22.5 - 67.5	104	1316538	5.600	11.605	0.483
	East (E) 67.5 - 112.5	202	1538622	10.878	13.562	0.802
	Southeast (SE) 112.5 - 157.5	262	1302255	14.109	11.479	1.229
	South (S) 157.5 - 202.5	451	1585431	24.286	13.975	1.738
	Southwest (SW) 202.5 - 247.5	326	1442610	17.555	12.716	1.381
	West (W) 247.5 - 295.5	186	1542519	10.016	13.597	0.737
	Northwest (NW) 295.5 - 337.5	131	1074519	7.054	9.472	0.745
Wetness Index	2.5 - 5	690	4032369	37.157	35.545	1.045
	5 - 7.5	886	5640039	47.711	49.716	0.960
	7.5 - 10	180	1039959	9.693	9.167	1.057
	10 - 12.5	83	419157	4.470	3.695	1.210
	>12.5	18	213003	0.969	1.878	0.516
Stream Power Index	<0.22	308	3052873	16.586	26.910	0.616
	0.22 – 0.5	728	5567345	39.203	49.074	0.799
	0.5 - 3	821	2724513	44.211	24.016	1.841

Variable	Classes	No. of Landslide Pixels in Class	Total No. of Pixels in Class	Landslides Pixels (%)	Domain Pixels (%)	FR
Slope	0 – 5	50	715041	2.693	6.303	0.427
	5 – 15	403	3709152	21.702	32.695	0.664
	15 – 25	495	3948507	26.656	34.805	0.766
	25 – 35	544	2222946	29.295	19.595	1.495
	35 – 63	365	749061	19.655	6.603	2.977
Rainfall	1300 - 1450	117	1032885	6.300	9.105	0.692
	1450 - 1600	1418	5686020	76.360	50.121	1.524
	1600 - 1750	322	4625775	17.340	40.775	0.425
North Exposure	Other Direction	1417	7329294	76.306	64.605	1.181
	North Facing	440	4015413	23.694	35.395	0.669
East Exposure	Other Direction	1635	9811089	88.045	86.482	1.018
	East Facing	222	1533618	11.955	13.518	0.884
Profile Curvature	< -0.005	150	686763	8.078	6.054	1.334
	-0.005 - 0.005	1672	10122858	90.038	89.230	1.009
	>0.005	35	535086	1.885	4.717	0.400
Plan Curvature	< -0.01	265	1714158	14.270	15.110	0.944
	-0.01 - 0.01	1515	7672833	81.583	67.634	1.206
	> 0.01	77	1957716	4.146	17.257	0.240
Distance to Roads	0 - 100	558	461763	31.886	4.104	7.770
	100 - 200	85	401976	4.857	3.572	1.360
	200 - 300	55	402696	3.143	3.579	0.878
	300 - 400	78	347220	4.457	3.086	1.444
	400 - 500	14	366291	0.800	3.255	0.246

Variable	Classes	No. of Landslide Pixels in Class	Total No. of Pixels in Class	Landslides Pixels (%)	Domain Pixels (%)	FR
	>500	960	9272484	54.857	82.404	0.666
Distance to Rivers	0 - 100	171	650286	9.727	5.783	1.682
	100 - 200	30	668232	1.706	5.943	0.287
	200 - 300	74	729045	4.209	6.484	0.649
	300 - 400	76	627948	4.323	5.585	0.774
	400 - 500	79	668448	4.494	5.945	0.756
	>500	1328	7900245	75.540	70.261	1.075

4.3.3 Binary Logistic Regression (BLR)

4.3.3.1 Check for correlation between the continuous variables

All correlation coefficients fell between -0.7 and 0.7 (see **Table 4-4**), indicating generally weak relationships among variables and a low likelihood of multicollinearity. This aligns with the VIF results, which also confirmed acceptable collinearity levels.

Table 4-4: Correlation between the continuous variables

Variables	Elevation	Rainfall	WI	Slope	SPI	Distance to Roads	Distance to Rivers	Profile Curvature	Plan Curvature
Elevation	1.000								
Rainfall	0.018	1.000							
WI	-0.039	-0.022	1.000						
Slope	-0.012	0.008	-0.481	1.000					
SPI	-0.070	-0.060	0.337	0.228	1.000				
Distance to Roads	0.038	0.281	-0.002	-0.139	-0.156	1.000			
Distance to Rivers	0.040	0.051	-0.046	0.152	0.068	0.060	1.000		
Profile Curvature	0.138	0.079	-0.281	0.124	-0.298	0.080	0.074	1.000	
Plan Curvature	0.025	-0.011	-0.341	0.079	-0.407	0.068	0.048	0.223	1.000

The strongest correlations occurred between WI and slope ($r = -0.481$), WI and SPI ($r = 0.337$), and SPI with both profile curvature ($r = -0.298$) and plan curvature ($r = -0.407$). These patterns are expected given how the variables are derived: WI reflects both slope and upslope contributing area, steeper slopes drain more rapidly, reducing moisture accumulation, while SPI incorporates slope and flow accumulation, explaining its positive association with WI and negative association with curvature. Curvature influences flow convergence and divergence, which directly affects erosion processes captured by SPI. Although these variables are conceptually linked, the correlations were not strong enough to pose problems for the regression. Overall, the correlation structure supports the inclusion of all variables in the BLR model.

4.3.3.2 Check if the continuous independent variables are linearly related to the log odds

To satisfy the assumptions of BLR, each continuous predictor must exhibit a linear relationship with the log-odds of the outcome. This was assessed by creating interaction terms between each variable and its natural logarithm and testing their significance (**Table 4-5**). A p-value below 0.05 indicates a breach of the linearity assumption.

Table 4-5: Linear relationship to the log odds

Variable by Natural Log (LN) of Variable	Significance
LN Elevation by LN Elevation	0.736
LN Profile Curvature by Profile Curvature	0.160
LN Plan Curvature by Plan Curvature	0.240
LN Rainfall by Rainfall	0.067
LN WI by WI	0.912
LN Slope by Slope	0.836
LN SPI by SPI	0.342
LN Distance to Roads by Distance to Roads	0.361
LN Distance to Rivers by Distance to Rivers	0.985

All interaction terms returned p-values above 0.05, ranging from 0.067 (Rainfall) to 0.985 (Distance to Rivers), indicating no significant departures from linearity. The linearity assumption was therefore considered met for all continuous variables included in the model.

4.3.3.3 Integrated BLR and FR Results

The BLR results are summarised in this subsection, with the full output provided in

Appendix C. In every step, estimation stopped once there were no longer changes being made to the parameter estimates, which confirmed that the model had successfully achieved convergence. The final BLR model (See **Table 4-6**) kept six predictor variables, although only five predictors were significant.

Table 4-6: Predictor variables retained in the final BLR model, with coefficients and significance levels showing their influence on landslide occurrence

Variable	B (Coefficient)	Sig. (p-value)
Elevation	0.289	0.087
Rainfall	-0.450	0.012
Slope	0.803	<.001
Distance to Roads	-0.758	<.001
Profile Curvature	-0.462	0.008
East Exposure	0.984	0.033

Variable(s) entered on step 1: Elevation, Rainfall, WI, Slope, SPI, Distance to Roads, Distance to Rivers, Profile Curvature, Plan Curvature, East Exposure, North Exposure, Aspect.

Elevation showed a positive coefficient in the BLR model ($B = 0.289$, $p = 0.087$), echoing the FR pattern where the 2600–3000 m class exhibited the strongest association with landslides. Although not statistically significant at the 95% level, this trend is consistent with studies noting that higher elevations tend to coincide with steeper slopes which are susceptible to landslides (Çellek, 2020; Yilmaz et al., 2012). Slope emerged as a strong predictor in the BLR model ($B = 0.803$, $p < 0.001$), indicating that steeper gradients substantially increase the odds of landslide occurrence. This aligns closely with the FR results, where the steepest slopes (35–63°) recorded the highest susceptibility. These findings are consistent with literature emphasising slope angle as a primary determinant of stability in mountainous terrain (Corominas et al., 2014; Mind'je et al., 2020; Sharma et al., 2014). For profile curvature, both the FR and BLR analysis showed that concave profile curvature had the highest susceptibility, reflecting its tendency to accumulate moisture and promote saturation (Chen et al., 2018; Yilmaz et al., 2012). Aspect-related patterns also illustrate the complementary strengths of the two methods. FR results showed that south-facing slopes followed by the east facing slopes were prone to failure, while the BLR model, identified east-facing slopes ($B = 0.984$, $p = 0.033$). This suggests that once other variables are accounted for, finer-scale directional effects, possibly related to solar radiation or soil moisture dynamics, become more apparent. Proximity to roads was one of the most influential predictors, with the FR analysis showing high susceptibility within 100 m of roads and the BLR model confirming a significant negative relationship ($B = -0.758$, $p < 0.001$). This reflects the destabilising effects of road cuts, excavation, and altered drainage pathways in steep terrain, a pattern widely reported in Rwanda and other tropical montane regions (Mind'je et al., 2020; Nsengiyumva et al., 2018).

Rainfall produced one of the most notable findings. While rainfall is widely recognised as a major trigger of landslides in Rwanda (Nahayo et al., 2019; Nsengiyumva et al., 2018; Silalahi et al., 2019), both FR and BLR results showed that the areas receiving the highest rainfall levels in Nyungwe were comparatively stable. The BLR model identified a significant negative relationship ($B = -0.450$, $p = 0.012$), and the FR analysis showed the lowest susceptibility in the highest rainfall class. Further inspection revealed that these high-rainfall zones coincide with gentler slopes and greater distances from roads, conditions that the BLR model identifies as stabilising. An additional consideration is the coarse spatial resolution of the CHIRPS rainfall dataset (5 km), which smooths fine-scale variability and causes rainfall values to represent broad environmental zones rather than slope-specific conditions.

4.4 Landslide detection performance of the Tropical Moist Forest (TMF) product

4.4.1 Overall TMF Product Performance

The comparison between the landslide inventory and the TMF product provided an initial assessment of TMF's ability to detect landslide-related forest disturbance. Out of the 107 mapped landslides, 54 were detected by TMF and 53 were missed, giving an overall detection rate of 50.5%. This means that TMF identified just over half of the landslides in the study area (**Table 4-7)**. This highlights a notable limitation in the sensitivity of the TMF product in identifying landslide disturbance, particularly in forested tropical environments.

Table 4-7: Confusion matrix

Metric	Value
True Positives (TP)	54
False Negatives (FN)	53
False Positives	N/A
True Negatives	N/A
Error of Omission	0.495
Error of Commission	N/A
Producer's Accuracy	0.505
User's Accuracy	1

An understanding of the distribution of landslide areas within the inventory is essential before evaluating whether TMF detection varies systematically with landslide size. The mapped landslides range from 62 m² to 14,532 m² (see **Figure 4-3**). This plot of landslide area distributions provides two important insights. The inventory is dominated by small to medium sized landslides, which are inherently more difficult for TMF to detect due to their limited spatial footprint. Secondly, TMF should reliably detect larger landslides.

To assess whether landslide area influences the likelihood of detection by the TMF product, the area distributions of detected and undetected landslides were examined separately (see **Figure 4-4**).

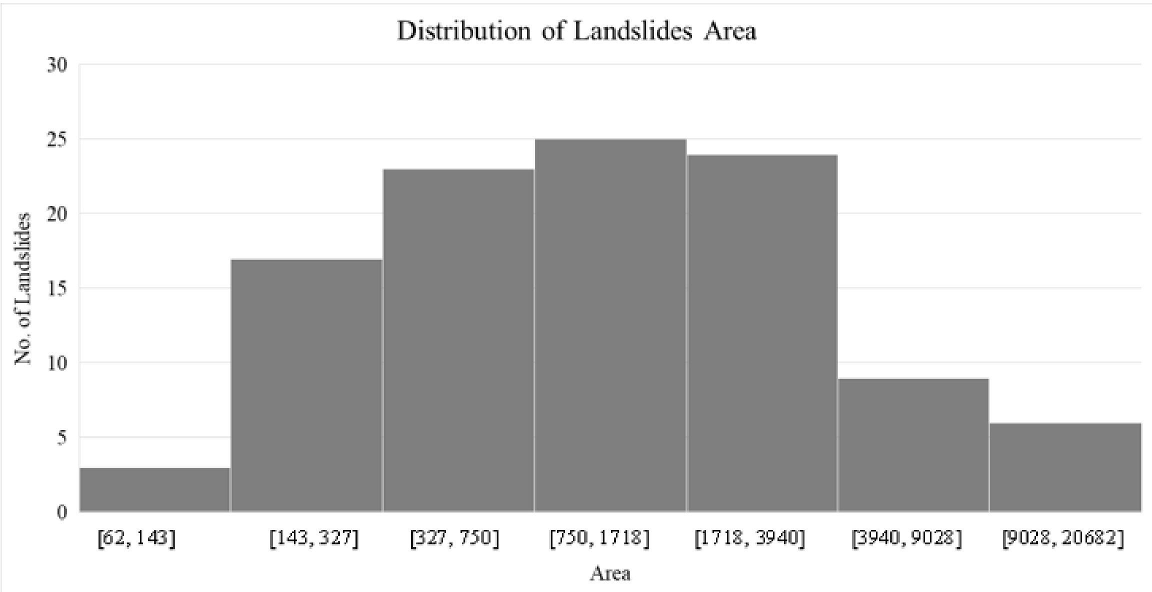

Figure 4-3: Histogram of landslide areas.

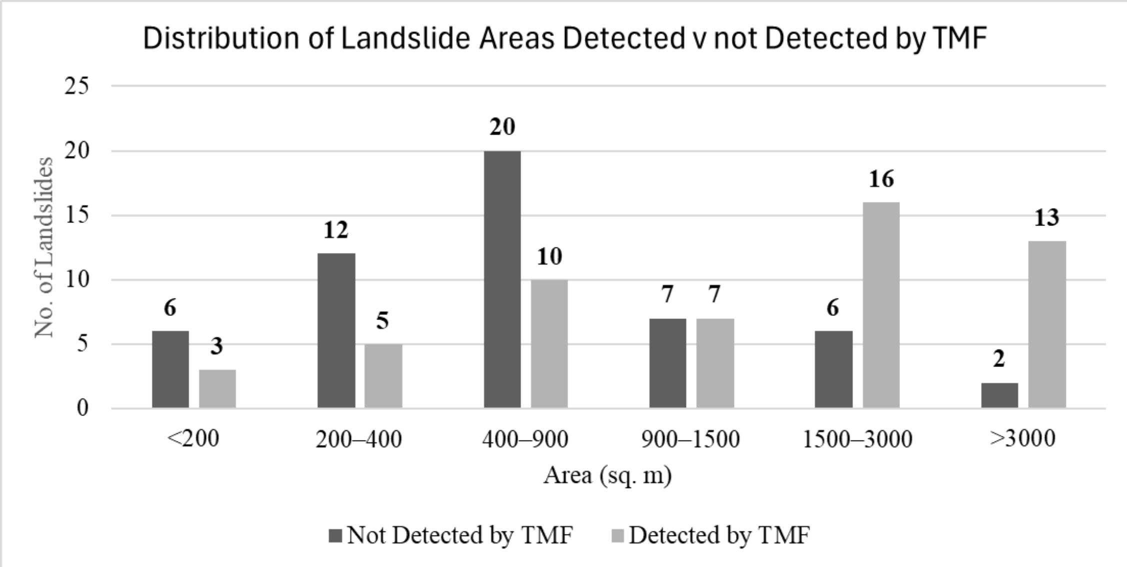

Figure 4-4: Histogram of area for TMF detected v non-detected landslides

Detected landslides tend to occupy the upper end of the size range, with many events exceeding 900 m² and several extending beyond 15,000 m². In contrast, undetected landslides are predominantly small, with most events falling below 900 m², which represents the area of a single 30 m Landsat pixel. This indicates that TMF omissions occur predominantly among smaller landslides and aligns with the expectation that larger disturbances produce stronger spectral signals and affect multiple Landsat pixels, increasing the likelihood of detection. Therefore, landslide size is a key determinant of TMF detection performance.

4.4.2 Pixel-level TMF detection of landslide-related forest disturbance

Detection years ranged from 2003 to 2024, with a strong temporal clustering in the last decade. Of the 54 detected landslides, 72% were first detected after 2017, and 48% were detected between 2020 and 2024. Only 6% of detections occurred before 2010.

Disturbance durations, defined as the number of consecutive years a pixel remained in class 2 or 3 after detection, varied across the dataset from 1 to 10 years. Short-duration disturbances (1-2 years) accounted for 11% of detected landslides, while the majority (63%) exhibited disturbance durations of 3-6 years. A further 22% remained disturbed for 7-10 years, and 4% exceeded 10 years. However, because 2024 is the final year of TMF data, disturbance cannot be concluded for landslides that remained in class 2 or 3 in 2024, as at the time of their transition. For these landslides, recovery may occur beyond 2024 but cannot be observed within the available TMF time series.

The capacity of the TMF product to identify landslide-induced disturbances is influenced by a range of spatial, temporal, and methodological factors inherent to the dataset. Rwanda's tropical location makes it highly susceptible to persistent cloud cover, especially during the wet seasons. Such conditions present a major challenge for remote sensing applications and are widely acknowledged as a limitation in tropical regions more generally (Nkundabose et al., 2021). The issue is further compounded by the fact that landslides are most likely to occur during the wet season, when obtaining cloud-free imagery is most difficult. Moreover, optical imagery tends to be clearer and more readily available during the dry months (Gutkin et al., 2023). The TMF framework incorporates a cloud-screening step during its initial phase of analysis. At this stage, single-date images are classified into categories of potential moist forest cover, potential disturbance, or invalid observations such as cloud and cloud shadow (Vancutsem et al., 2021). Although Landsat provides a nominal 16-day revisit interval, the practical observation frequency over tropical regions like Rwanda is far lower. Persistent cloud cover restricts the number of clear-sky scenes, and some studies note that analysts often resort to imagery with up to 50% cloud cover because scenes with less than 20% cloud contamination are rare ((Ndungu & Zentai, 2024). Therefore, in regions with frequent cloud cover, such as Rwanda, the number of usable Landsat observations is significantly reduced (Vancutsem et al., 2021). Temporal density is further reduced in the earlier Landsat missions, which acquired fewer scenes over Central Africa. After 2003, the Landsat 7 ETM+ SLC-off malfunction introduced additional wedge-shaped data gaps, removing roughly 22% of each scene and further diminishing usable coverage (Basnet & Vodacek, 2015). Therefore, there is the possibility that certain landslides may be overlooked particularly due to temporal gaps and the frequency of observations, as the number of valid Landsat acquisitions for a given pixel directly influences the confidence with which disturbances can be detected. Vancutsem et al. (2021) validated the TMF product using sample plots with at least one reliable Landsat interpretation derived from cloud-free scenes and images unaffected by sensor artefacts. The single-date classification approach achieved an overall accuracy of 91.4%, with Africa showing the highest regional accuracy at 94.6%. This indicates that when a clear, unobstructed Landsat observation is available, the TMF algorithm is capable of identifying forest disturbance with high reliability. Consequently, many missed events in this study are likely attributable to limited valid observations associated with cloud cover.

Although the TMF product benefits from Landsat Collection 2 improvements (European Commission, 2024b), areas with historically sparse data remain susceptible to omission errors, meaning that some disturbances may not be captured. One way to address cloud-related gaps as the TMF dataset continues to expand is by integrating radar imagery, such as that provided by Synthetic Aperture Radar (SAR) sensors. Unlike optical sensors, SAR uses microwave signals, enabling all-weather, day-and-night observation of the Earth's surface (Meng et al., 2024). For example, the European Space Agency's Sentinel-1 mission delivers consistent imagery every 6–12 days at 10-meter spatial resolution, making it valuable for detecting forest disturbances that optical sensors might miss due to persistent clouds (Reiche et al., 2021). Furthermore, radar data can reveal structural changes in vegetation, including tree loss or reductions in biomass, providing complementary information to optical imagery and enhancing the overall reliability of forest monitoring and small-scale landslide detection (Dostálová et al., 2021; Tzouvaras et al., 2020).

The TMF dataset is derived from Landsat satellite imagery, which operates at a spatial resolution of 30 meters (Acker et al., 2014; Markham et al., 2018; Vancutsem et al., 2021). While this resolution and the available data archive provide a valuable long-term record of forest change at a global scale, it also introduces certain limitations in detecting fine-scale disturbances. Any disturbance that affects less than the area of a full pixel, for instance, the removal of a single tree or a landslide narrower than 30 meters, may not generate a strong enough spectral signal to be recognised as a change event. This supports this study's results, where TMF omissions occur predominantly among smaller landslides. This limitation is closely related to the "mixed pixel" effect, in which the spectral signature of a single pixel is influenced by multiple land cover types rather than representing a single, homogeneous surface (Nghiyalwa et al., 2021; Perikamana et al., 2024). As a result, when small disturbances occur, their signal can be diluted by the unaffected portions of the pixel, making them indistinguishable to the sensor. Even in instances where several trees are removed within a limited space, the impact may still be too minor relative to the overall pixel area to be detected by Landsat sensors and, by extension, the TMF product.

In contrast, large-scale events that significantly reduce canopy cover across multiple adjacent pixels, such as extensive landslides or clear-cutting, tend to produce stronger spectral shifts that are more readily detected (Acker et al., 2003). Detection becomes highly reliable for events exceeding ~3000 m^2, as these disturbances span several pixels and generate clear spectral change. This pattern confirms that pixel size is a key driver of omission errors, particularly for small and spatially confined landslides

Spectral Confusion with other nearby disturbances or classes also contributes to the poor performance. The TMF product is designed to detect disturbances caused by activities such as logging, agricultural expansion, and infrastructure development (European Commission, 2024b). However, landslide scars can produce spectral signals that look similar to nearby clearings or may intersect or occur alongside roads. Because TMF applies spatial filters and classification rules to reduce noise and ignore short-term fluctuations, some landslide events, especially small or isolated ones, may be unintentionally excluded from detection (European Commission, 2024b). This can make it challenging to capture all landslides using the TMF dataset. Of the 29 landslides in the inventory which occurred alongside roads, 11 were not detected as a degradation or deforested, as illustrated in **Figure 4-5**.

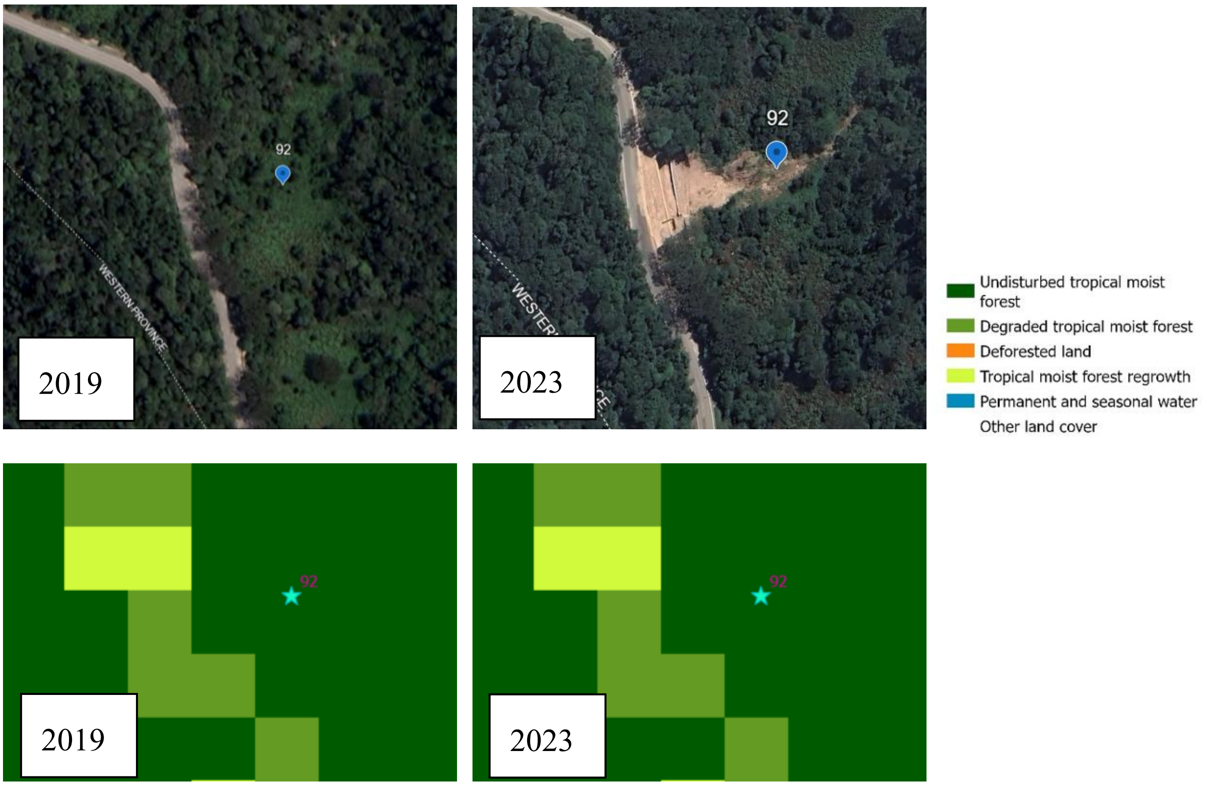

Figure 4-5: Landslide occurring directly alongside a road, illustrating how its proximity to the road led to it being missed by the TMF algorithm due to spectral confusion and spatial filtering

A hybrid transition map at 10-meter resolution has been developed for the period 1990–2022, integrating forest disturbance detections from Sentinel-2 for the year 2022 (European Commission, 2024b). With its 10-meter spatial resolution and 5-day revisit frequency, Sentinel-2 provides finer detail, enabling the identification of small landslides that may be missed by coarser sensors (Mulas et al., 2020; Notti et al., 2022). Integrating Sentinel-2 into TMF data improves the delineation of degraded forests and disturbance edges, including linear features such as roads (European Commission, 2024b). Some small-scale disturbances detected in 2022 using Sentinel-2 may have occurred in earlier years but were undetected by Landsat due to its lower spatial resolution. Plans are underway to leverage the full historical Sentinel-2 archive to produce an enhanced version of this hybrid transition map (European Commission, 2024b). Furthermore, integrating Sentinel-2 into annual TMF maps could improve overall detection accuracy and reduce timing uncertainties, due to its high temporal resolution (Xu et al., 2022).

4.5 Post-Landslide vegetation recovery

Post-landslide vegetation recovery forms an integral part of tropical moist forest ecosystems characterised by a complex relationship between natural disturbances, site conditions, and ecological succession (Crausbay & Martin, 2016; Freund & Silman, 2023). Within the TMF framework, regrowth is defined as a two-step transition, first from forest to deforested land, and then from deforested land to regrown forest. To avoid misclassification with shifting cultivation or other short-term land uses, TMF requires that a minimum of three years of continuous forest cover be present before a pixel is labelled as regrowth (Vancutsem et al., 2021). This temporal threshold ensures that regrowth classifications reflect genuine forest recovery rather than transitional vegetation change. A major limitation of the analysis is that 2024 is the final year of TMF data (see **Appendix D**). For landslides that remained in class 2 or 3 in 2024, disturbance durations are right-censored, meaning that the true duration of canopy disturbance is longer than the observed value. Recovery may occur beyond 2024 but cannot be assessed until future TMF updates become available. As a result, the disturbance durations reported here should be interpreted as minimum estimates rather than complete disturbance histories.

Regrowth (class 4) was detected in only a small subset of landslides, reflecting the limited number of cases where canopy recovery progressed sufficiently to produce a spectral signature consistent with TMF's regrowth class. Only four landslides (7.4%) exhibited a transition from class 2 or 3 to class 4 (see **Appendix D**). These cases represent the spectral evidence of canopy recovery within the TMF observation window. All four landslides exhibited complete disturbance-regrowth cycles, transitioning from undisturbed forest to deforestation and subsequently to regrowth. Landslide 33 showed a short regrowth period beginning in 2024, while landslide 43 exhibited a regrowth phase between 2018 and 2023.

The two landslide events, Landslide 98 and 126, produced the longest lasting regrowth evidence, exhibiting continuous growth for four and seven years respectively. The observed regrowth traces were only visible 5 to 10 years post-disturbance and aligning with early-stage successional development of tropical montane forests (Crausbay & Martin, 2016; Freund & Silman, 2023). However, TMF represents a regrowth class based on spectral properties indicative of recovering forest and does not represent a full structural or biomass recovery. True ecological recovery including canopy height and biomass accumulation can take multiple decades (Freund & Silman, 2023); thus, TMF only records the earliest, high contrast phase of recovery instead of the entire ecological trajectory.

Partial canopy regeneration was also seen in four other landslides where there were transitions from Class 3 to Class 2. This suggests fewer consecutive disturbances and that while the vegetation in these areas has started to grow back, they have not yet achieved the level of vegetative density required to be classified as regrowing forest according to the TMF classification. In each of these four cases, the transition from Class 3 to Class 2 took place in 2024 following one or more years in Class 3. It appears this is very early detection of recovery near the end of the TMF data collection period. All other landslides identified through TMF remained in either Class 2 or Class 3 in 2024. Therefore, recovery could potentially occur beyond the length of the observational record.

Disturbances caused by landslides are among many agents affecting both the composition and structure of Nyungwe Forest Reserve's ecosystem. The Nyungwe Forest Reserve is characterised by steep slopes, varied soils, and significant climate and atmospheric gradients along altitude (Mlotha, 2018). Landslides create canopy gaps that lead to promotion of primary succession. Primary succession promotes new establishment of species within newly formed gaps leading to the beginning stages of forest recovery (Crausbay & Martin, 2016). Although succession will follow a similar path across different disturbances, it will vary depending upon factors related to local species pools, soil stability and presence of residual plants. Residual plants help accelerate the recovery process (Freund et al., 2021).

An important aspect of Nyungwe Forest Reserve’s successional pathways is the quick colonisation of the newly opened canopy gaps by the native yet invasive liana *Sericostachys scandens*. The species produces large mono-dominant patches that inhibit tree regeneration and affect the way succession occurs. Often, they delay or direct the recovery process of the forest (Bizuru et al., 2015; Scholte et al., 2010; Van der Heyden, 2016). Alongside lianas, early successional tree species also play a critical role. *Macaranga kilimandscharica* is particularly a dominant pioneer species found across Nyungwe. One study estimated that *Macaranga kilimandscharica* occurred in about 42% of the vegetation communities in the reserve (Mlotha, 2018). This species contributes significantly to post-disturbance recovery by establishing itself quickly and its persistence in establishment during recovery trajectories. The above information illustrates the characteristics of post-landslide recovery in Nyungwe Forest Reserve. Landslides open up canopy gaps creating opportunity for successional processes which could lead to restoration of forest structure and function. However, colonisation by highly competitive native species such as *Sericostachys scandens*, and/or establishment of pioneer trees like *Macaranga kilimandscharica*, creates opportunities for alternate successful pathways potentially slowing or reshaping forest recovery. These dynamics may slow or alter canopy closure, prolonging the period during which landslide scars remain spectrally distinct and therefore detectable by TMF. Therefore, understanding post-landslide regrowth requires both long-term field studies along with long term remote sensing data to understand all aspects of outcomes after landslides in complex tropical montane ecosystems like Nyungwe Forest Reserve.

5 Conclusion

5.1 Research Objectives and Summary of Findings

This research set out to advance understanding of landslide occurrence and post-landslide recovery dynamics in Nyungwe Forest Reserve by integrating multi-temporal landslide mapping, environmental predictor analysis, and a pixel-level evaluation of TMF product. This aim was supported by four objectives:

1. To compile a multi-temporal landslide inventory for Nyungwe Forest Reserve (2000 to 2024) using high-resolution imagery.
2. To assemble a suite of environmental and geomorphological predictor variables relevant to landslide processes in Afromontane landscapes and determine the relationship between these variables and landslide occurrence.
3. To conduct a pixel-level assessment of the Tropical Moist Forest (TMF) product to evaluate its ability to detect landslide-induced forest disturbance.
4. To examine post-landslide forest recovery patterns using the TMF product.

Together, the four objectives addressed complementary components of the landslide and forest interaction system, producing an assessment of both the drivers of landsliding and their detectability using satellite-based forest monitoring products.

The first objective resulted in the development of a multi-temporal landslide inventory spanning 2000 to 2024, compiled from high-resolution optical imagery. This inventory represents the most complete record of landslide activity in Nyungwe Forest Reserve to date, capturing both spatial patterns and temporal variability across nearly a quarter century.

The second objective focused on assembling a suite of environmental and geomorphological predictor variables relevant to landslide processes in Afromontane landscapes and more specifically Rwanda and quantifying their relationship with mapped landslides. Overall, the FR and BLR analyses showed that landslide occurrences in Nyungwe Forest Reserve are primarily controlled by steep slopes, rainfall, proximity to roads, profile curvature and exposure of slopes to the east. FR highlighted where landslides cluster within specific variable classes, while BLR clarified which predictors remained significant when considered together. Slope consistently emerged as the strongest driver in both approaches, and distance to roads was confirmed as a major anthropogenic control. Although FR suggested roles for wetness-related indices, these effects weakened or disappeared in the BLR model. The influence of rainfall was found to be largely mediated through terrain characteristics. Together, the two methods provide an understanding of landslide susceptibility, with FR revealing spatial patterns and BLR identifying the most robust predictors of landslide probability.

The third objective evaluated the ability of the TMF product to detect landslide-induced forest disturbance at the pixel level. The analysis demonstrated that TMF detects medium-to-large landslides, but under-detects small failures. Detection was strongly size-dependent, with most TMF-detected landslides exceeding the Landsat pixel footprint. Disturbance durations ranged from 1 to 10 years, but the majority of trajectories were right-censored because 2024 is the final year of TMF data, meaning that disturbance was still ongoing for most detected landslides. The study explored the factors influencing TMF's detection performance. Key drivers of the omission are mainly linked to pixel resolution, temporal rules regarding classifications of disturbances; potential data gaps within historical Landsat observation records due to cloud cover; and spectral confusions with other types of disturbances. Combined, these issues illustrate why there were omissions as well as the difficulties in detecting landslide disturbances through use of products developed from medium-resolution optical satellites.

The fourth objective was to look at post-landslide forest regrowth using TMFs regrowth and degradation classes. There were only four landslides where complete disturbance and regrowth cycles could be identified. All of these landslides displayed multi-year regrowth trends that indicated continued canopy development after initial disturbance. Four additional landslides demonstrated partial canopy regrowth, transitioning from being deforested into degraded forests. This indicates early stages of vegetation return that has not achieved the spectral values for TMF's regrowth class. The majority of landslide disturbance trajectories are right-censored (i.e., indicate that most of the disturbance recovery process remains uncompleted) based upon the TMF data available. Post-disturbance recovery in Nyungwe Forest Reserve likely involves rapid colonisation by pioneering species such as *Macaranga kilimandscharica,* and the native liana *Sericostachys scandens*. While these species promote canopy closure, they can also suppress late-successional regeneration, changing recovery pathways. As a result, the outcome of post-disturbance recovery may not necessarily involve a return to undisturbed mature forest; instead, it can lead to new community structures that have different functional properties than undisturbed mature forest. Therefore, TMF captures the onset of recovery to a forested state but not its full ecological trajectory, which is expected to unfold over decades in tropical montane forests.

Overall, this study illustrates the benefits of combining high-resolution landslide mapping for use in developing inventories, evaluating environmental and geomorphological factors that predict landslide occurrence, and utilising remote sensing-derived products of forest disturbance to better understand the ways in which geomorphic processes interact with forest ecosystems in Afromontane regions. In addition, the multi-temporal landslide database and landslide predictive model that were generated may prove useful for enhancing landslide hazard assessments; likewise, the TMF validation demonstrates the situations in which this satellite-derived forest disturbance product can identify impacts caused by landslide activity. Ultimately, the findings of this study illustrate the necessity of conducting extended time frame studies to document all phases of forest regeneration after a series of post-disturbance events occur.

5.2 Further Research

This research has shown both the utility and limitations of the TMF product for detecting landslide activity in tropical montane rainforests. Although TMF is a valuable resource, providing long-term data sets for broad-scale observation of forest disturbances, it relies upon Landsat imagery and utilises strictly defined temporal constraints, which limits its ability to capture localised and transient events (i.e., small landslides). The findings of this research have emphasised the need for additional methodologies to support TMF, including combinations of higher spatial and temporal resolution (e.g., Sentinel-2 and Sentinel-1) remote-sensing data, in order to increase the accuracy of identifying disturbances. Through mitigating these limitations, future investigations can advance knowledge regarding forest disturbance, including landslide dynamics and how they influence structural composition and resilience of tropical moist forests such as Nyungwe Forest Reserve.

References

Abeysiriwardana, H. D., & Gomes, P. I. (2022). Integrating vegetation indices and geo-environmental factors in GIS-based landslide-susceptibility mapping: using logistic regression. *Journal of Mountain Science*, *19*(2), 477–492.

Acker, J., Williams, R., Chiu, L., Ardanuy, P., Miller, S., Schueler, C., Vachon, P. W., & Manore, M. (2003). Remote Sensing from Satellites. In R. A. Meyers (Ed.), *Encyclopedia of Physical Science and Technology (Third Edition)* (pp. 161–202). Academic Press. https://doi.org/https://doi.org/10.1016/B0-12-227410-5/00938-8

Acker, J., Williams, R., Chiu, L., Ardanuy, P., Miller, S., Schueler, C., Vachon, P. W., & Manore, M. (2014). Remote sensing from satellites☆. *Reference module in earth systems and environmental sciences*.

Akayezu, P., Ndagijimana, I., Dushimumukiza, M. C., Bernhard, K. P., & Groen, T. A. (2022). Community livelihoods and forest dependency: Tourism contribution in Nyungwe National Park, Rwanda. *Frontiers in Conservation Science*, *3*, 1034144.

Ariza-López, F. J., Rodriguez-Avi, J., & Alba-Fernandez, M. (2018). Complete control of an observed confusion matrix. IGARSS 2018-2018 IEEE International Geoscience and Remote Sensing Symposium,

Arrogante-Funes, P., Bruzón, A. G., Álvarez-Ripado, A., Arrogante-Funes, F., Martín-González, F., & Novillo, C. J. (2024). Assessment of the regeneration of landslides areas using unsupervised and supervised methods and explainable machine learning models. *Landslides*, *21*(2), 275–290.

Barsi, Á., Kugler, Z., László, I., Szabó, G., & Abdulmutalib, H. (2018). Accuracy dimensions in remote sensing. *The International Archives of the Photogrammetry, Remote Sensing and Spatial Information Sciences*, *42*, 61–67.

Basnet, B., & Vodacek, A. (2015). Tracking Land Use/Land Cover Dynamics in Cloud Prone Areas Using Moderate Resolution Satellite Data: A Case Study in Central Africa. *Remote Sensing*, *7*(6), 6683–6709.

Bizuru, E., Nshutiyayesu, S., Nsabagasani, C., Tuyisingize, D., & Uwayezu, E. (2015). Study to establish a national list of threatened terrestrial ecosystem and species in need of protection in Rwanda. In: Kigali: Rwanda Environment Management Authority.

Buma, B., & Pawlik, Ł. (2021). Post-landslide soil and vegetation recovery in a dry, montane system is slow and patchy. *Ecosphere*, *12*(1), Article e03346. https://doi.org/10.1002/ecs2.3346

Cellek, S. (2021). The effect of aspect on landslide and its relationship with other parameters. In *Landslides*. IntechOpen.

Çellek, S. (2020). Morphological parameters causing landslides: A case study of elevation. *Bulletin of the Mineral Research and Exploration*, *162*(162), 197–224.

Chen, C. F., Li, C. F., Huang, C. M., Lin, H. Y., & Zelený, D. (2022). Secondary succession on landslides in submontane forests of central Taiwan: Environmental drivers and restoration strategies. *Applied Vegetation Science*, *25*(1), e12635.

Chen, W., Chai, H., Sun, X., Wang, Q., Ding, X., & Hong, H. (2016). A GIS-based comparative study of frequency ratio, statistical index and weights-of-evidence models in landslide susceptibility mapping. *Arabian Journal of Geosciences*, *9*(3), 204.

Chen, W., Pourghasemi, H. R., & Naghibi, S. A. (2018). Prioritization of landslide conditioning factors and its spatial modeling in Shangnan County, China using GIS-based data mining algorithms. *Bulletin of Engineering Geology and the Environment*, *77*(2), 611–629.

Climate Hazard Center. (2025). *CHIRPS: Rainfall Estimates from Rain Gauge and Satellite Observations*. Retrieved 25 May 2025 from https://www.chc.ucsb.edu/data/chirps

Cohen, D., & Schwarz, M. (2017). Tree-root control of shallow landslides. *Earth Surface Dynamics*, *5*(3), 451–477.

Conforti, M., Aucelli, P. P., Robustelli, G., & Scarciglia, F. (2011). Geomorphology and GIS analysis for mapping gully erosion susceptibility in the Turbolo stream catchment (Northern Calabria, Italy). *Natural Hazards*, *56*(3), 881–898.

Corominas, J., van Westen, C., Frattini, P., Cascini, L., Malet, J.-P., Fotopoulou, S., Catani, F., Van Den Eeckhaut, M., Mavrouli, O., & Agliardi, F. (2014). Recommendations for the quantitative analysis of landslide risk. *Bulletin of Engineering Geology and the Environment*, *73*, 209–263.

Crausbay, S. D., & Martin, P. H. (2016). Natural disturbance, vegetation patterns and ecological dynamics in tropical montane forests. *Journal of Tropical Ecology*, *32*(5), 384–403. https://doi.org/10.1017/S0266467416000328

Creswell, J. W. (2009). Research design-qualitative, quantitative, and mixed methods approaches. *SAGE, Ca; ofprnia*.

Delgado Isasi, L., & Marín Briano, V. (2020). Ecosystem services and ecosystem degradation: environmentalist’s expectation.

Depicker, A., Govers, G., Jacobs, L., Vanmaercke, M., Uwihirwe, J., Campforts, B., Kubwimana, D., Mateso, J.-C. M., Bibentyo, T. M., & Nahimana, L. (2024). Mobilization rates of landslides in a changing tropical environment: 60-year record over a large region of the East African Rift. *Geomorphology*, *454*, 109156.

Depicker, A., Jacobs, L., Delvaux, D., Havenith, H.-B., Mateso, J.-C. M., Govers, G., & Dewitte, O. (2020). The added value of a regional landslide susceptibility assessment: The western branch of the East African Rift. *Geomorphology*, *353*, 106886.

Dislich, C., & Huth, A. (2012). Modelling the impact of shallow landslides on forest structure in tropical montane forests. *Ecological Modelling*, *239*, 40–53. https://doi.org/10.1016/j.ecolmodel.2012.04.016

Dostálová, A., Lang, M., Ivanovs, J., Waser, L. T., & Wagner, W. (2021). European wide forest classification based on sentinel-1 data. *Remote Sensing*, *13*(3), 337.

European Commission. (2024a). *Tracking long-term (1990-2023) deforestation and degradation in tropical moist forests*. Retrieved 04 November 2024 from https://forobs.jrc.ec.europa.eu/TMF

European Commission. (2024b). *Tropical Moist Forests product - Data Access*. Retrieved 22 May 2024 from https://forobs.jrc.ec.europa.eu/TMF/data

Filonchyk, M., Peterson, M. P., Zhang, L., Hurynovich, V., & He, Y. (2024). Greenhouse gases emissions and global climate change: Examining the influence of CO2, CH4, and N2O. *Science of The Total Environment*, 173359.

Foody, G. (2005). Local characterization of thematic classification accuracy through spatially constrained confusion matrices. *International Journal of Remote Sensing*, *26*(6), 1217–1228.

Foody, G. M. (2002). Status of land cover classification accuracy assessment. *Remote Sensing of Environment*, *80*(1), 185–201.

Freund, C. A., Clark, K. E., Curran, J. F., Asner, G. P., & Silman, M. R. (2021). Landslide age, elevation and residual vegetation determine tropical montane forest canopy recovery and biomass accumulation after landslide disturbances in the Peruvian Andes. *Journal of Ecology*, *109*(10), 3555–3571. https://doi.org/10.1111/1365-2745.13737

Freund, C. A., & Silman, M. R. (2023). Developing a more complete understanding of tropical montane forest disturbance ecology through landslide research. *Frontiers in Forests and Global Change*, *6*, Article 1091387. https://doi.org/10.3389/ffgc.2023.1091387

García-Rodríguez, M. J., Malpica, J. A., Benito, B., & Díaz, M. (2008). Susceptibility assessment of earthquake-triggered landslides in El Salvador using logistic regression. *Geomorphology*, *95*(3), 172–191. https://doi.org/https://doi.org/10.1016/j.geomorph.2007.06.001

Gholami, M., Ghachkanlu, E. N., Khosravi, K., & Pirasteh, S. (2019). Landslide prediction capability by comparison of frequency ratio, fuzzy gamma and landslide index method. *Journal of Earth System Science*, *128*(2), 42.

Gutkin, N., Uwizeyimana, V., Somers, B., Muys, B., & Verbist, B. (2023). Supervised classification of tree cover classes in the complex mosaic landscape of eastern Rwanda. *Remote Sensing*, *15*(10), 2606.

Guzzetti, F., Mondini, A. C., Cardinali, M., Fiorucci, F., Santangelo, M., & Chang, K.-T. (2012). Landslide inventory maps: New tools for an old problem. *Earth-Science Reviews*, *112*(1-2), 42–66.

Hansen, M. C., Potapov, P. V., Moore, R., Hancher, M., Turubanova, S. A., Tyukavina, A., Thau, D., Stehman, S. V., Goetz, S. J., & Loveland, T. R. (2013). High-resolution global maps of 21st-century forest cover change. *science*, *342*(6160), 850–853.

Hishamunda, S., Fashaho, A., Uwihirwe, J., Bugenimana, E. D., Musinga, C. M., & Munyandamutsa, P. (2024). Controlling soil erosion and landslides through ecosystem-based adaptation interventions in the hilly landscape of western Rwanda. *Soil Advances*, *2*, 100020.

Hosmer, D. W., Lemeshow, S., & Sturdivant, R. X. (2013). *Applied Logistic Regression: Third Edition* (3rd ed.). Wiley.

Huang, F., Mao, D., Jiang, S.-H., Zhou, C., Fan, X., Zeng, Z., Catani, F., Yu, C., Chang, Z., & Huang, J. (2024). Uncertainties in landslide susceptibility prediction modeling: a review on the incompleteness of landslide inventory and its influence rules. *Geoscience Frontiers*, 101886.

Huang, F., Yan, J., Fan, X., Yao, C., Huang, J., Chen, W., & Hong, H. (2022). Uncertainty pattern in landslide susceptibility prediction modelling: Effects of different landslide boundaries and spatial shape expressions. *Geoscience Frontiers*, *13*(2), 101317.

Huang, F., Ye, Z., Zhou, X., Huang, J., & Zhou, C. (2022). Landslide susceptibility prediction using an incremental learning Bayesian Network model considering the continuously updated landslide inventories. *Bulletin of Engineering Geology and the Environment*, *81*(6), 250.

IBM. (2024). *Logistic Regression*. Retrieved November 2025 from https://www.ibm.com/docs/en/spss-statistics/29.0.0?topic=SSLVMB_29.0.0/statistics_mainhelp_ddita/spss/regression/idh_lreg.html

Jakob, M. (2022). Landslides in a changing climate. In *Landslide hazards, risks, and disasters* (pp. 505–579). Elsevier.

Kayiranga, A., Kurban, A., Ndayisaba, F., Nahayo, L., Karamage, F., Ablekim, A., Li, H., & Ilniyaz, O. (2016). Monitoring forest cover change and fragmentation using remote sensing and landscape metrics in Nyungwe-Kibira park. *Journal of geoscience and Environment Protection*, *4*(11), 13–33.

Kintu, I. (2025). *Comparing the frequency ratio and the logisitic regression methods in identifying the environmental and geomorphological factors that most significantly contribute to landslide occurrence in Nyungwe Forest Reserve*. University of Twente.

Kirschbaum, D., Adler, R., Adler, D., Peters-Lidard, C., & Huffman, G. (2012). Global distribution of extreme precipitation and high-impact landslides in 2010 relative to previous years. *Journal of Hydrometeorology*, *13*(5), 1536–1551.

Law, Y. K., Lee, C. K., Chan, A. H., Mak, N. P., Hau, B. C., & Wu, J. (2024). Unveiling the role of forests in landslide occurrence, recurrence and recovery. *Journal of Applied Ecology*, *61*(9), 2033–2046.

Lee, H., Calvin, K., Dasgupta, D., Krinner, G., Mukherji, A., Thorne, P., Trisos, C., Romero, J., Aldunce, P., & Ruane, A. C. (2024). Climate change 2023 synthesis report summary for policymakers. *CLIMATE CHANGE 2023 synthesis report: summary for policymakers*.

Li, Nahayo, L., Habiyaremye, G., & Christophe, M. (2022). Applicability and performance of statistical index, certain factor and frequency ratio models in mapping landslides susceptibility in Rwanda. *Geocarto International*, *37*(2), 638–656.

Li, L., Lan, H., Strom, A., & Macciotta, R. (2022). Landslide longitudinal shape: a new concept for complementing landslide aspect ratio. *Landslides*, *19*(5), 1143–1163.

Liu, H., Mao, Z., Wang, Y., Kim, J. H., Bourrier, F., Mohamed, A., & Stokes, A. (2021). Slow recovery from soil disturbance increases susceptibility of high elevation forests to landslides. *Forest Ecology and Management*, *485*, Article 118891. https://doi.org/10.1016/j.foreco.2020.118891

Markham, B. L., Arvidson, T., Barsi, J. A., Choate, M., Kaita, E., Levy, R., Lubke, M., & Masek, J. G. (2018). 1.03 - Landsat Program. In S. Liang (Ed.), *Comprehensive Remote Sensing* (pp. 27–90). Elsevier. https://doi.org/https://doi.org/10.1016/B978-0-12-409548-9.10313-6

Meng, L., Yan, C., Lv, S., Sun, H., Xue, S., Li, Q., Zhou, L., Edwing, D., Edwing, K., & Geng, X. (2024). Synthetic aperture radar for geosciences. *Reviews of Geophysics*, *62*(3), e2023RG000821.

Mind'je, R., Li, L., Nsengiyumva, J. B., Mupenzi, C., Nyesheja, E. M., Kayumba, P. M., Gasirabo, A., & Hakorimana, E. (2020). Landslide susceptibility and influencing factors analysis in Rwanda. *Environment, Development and Sustainability*, *22*, 7985–8012.

Mitchell, J. C., Kashian, D. M., Chen, X., Cousins, S., Flaspohler, D., Gruner, D. S., Johnson, J. S., Surasinghe, T. D., Zambrano, J., & Buma, B. (2023). Forest ecosystem properties emerge from interactions of structure and disturbance. *Frontiers in Ecology and the Environment*, *21*(1), 14–23.

Mlotha, M. J. (2018). Analysis of land use/land cover change impacts upon ecosystem services in montane tropical forest of Rwanda: forest carbon assessment and REDD+ preparedness.

Monsieurs, E., Jacobs, L., Michellier, C., Basimike Tchangaboba, J., Ganza, G. B., Kervyn, F., Maki Mateso, J.-C., Mugaruka Bibentyo, T., Kalikone Buzera, C., & Nahimana, L. (2018). Landslide inventory for hazard assessment in a data-poor context: a regional-scale approach in a tropical African environment. *Landslides*, *15*, 2195–2209.

Mulas, M., Ciccarese, G., Truffelli, G., & Corsini, A. (2020). Integration of digital image correlation of Sentinel-2 data and continuous GNSS for long-term slope movements monitoring in moderately rapid landslides. *Remote Sensing*, *12*(16), 2605.

Nahayo, L., Kalisa, E., Maniragaba, A., & Nshimiyimana, F. X. (2019). Comparison of analytical hierarchy process and certain factor models in landslide susceptibility mapping in Rwanda. *Modeling Earth Systems and Environment*, *5*(3), 885–895.

NASA. (2024). *Global Landslide Catalog (Not updated)*. Retrieved 17 November 2024 from https://data.nasa.gov/Earth-Science/Global-Landslide-Catalog-Not-updated-/h9d8-neg4

Ndungu, L., & Zentai, L. (2024). *Land Use, Land Cover Classification in Rwanda using Machine Learning in Google Earth Engine*.

Nghiyalwa, H. S., Urban, M., Baade, J., Smit, I. P., Ramoelo, A., Mogonong, B., & Schmullius, C. (2021). Spatio-temporal mixed pixel analysis of savanna ecosystems: a review. *Remote Sensing*, *13*(19), 3870.

Nkundabose, J. P., Nshimiyimana, F., Twagirayezu, G., & Irumva, O. (2021). Employing remote sensing tools for assessment of land use/land cover (LULC) changes in Eastern Province, Rwanda. *American Journal of Remote Sensing*, *9*(1), 23–32.

Notti, D., Cignetti, M., Godone, D., & Giordan, D. (2022). Semi-automatic mapping of shallow landslides using free Sentinel-2 and Google Earth Engine. *Natural hazards and earth system sciences discussions*, *2022*, 1–34.

Nsengiyumva, J. B., Luo, G., Nahayo, L., Huang, X., & Cai, P. (2018). Landslide susceptibility assessment using spatial multi-criteria evaluation model in Rwanda. *International journal of environmental research and public health*, *15*(2), 243.

Oliveira, S. C., Zêzere, J. L., Garcia, R. A., Pereira, S., Vaz, T., & Melo, R. (2024). Landslide susceptibility assessment using different rainfall event-based landslide inventories: advantages and limitations. *Natural Hazards*, *120*(10), 9361–9399.

Peng, D., Yueren, X., Qinjian, T., & Wenqiao, L. (2021). Using Google Earth Images to Extract Dense Landslides Induced by Historical Earthquakes at the Southwest of Ordos, China

[Original Research]. *Frontiers in Earth Science*, *Volume 8 - 2020*. https://doi.org/10.3389/feart.2020.633342

Perera, E., Gunaratne, A., & Samarasinghe, S. (2022). Participatory landslide inventory (PLI): an online tool for the development of a landslide inventory. *Complexity*, *2022*(1), 2659203.

Perikamana, K. K., Balakrishnan, K., & Tripathy, P. (2024). Chapter 9 - Deep learning approach for monitoring urban land cover changes. In A. Kumar, P. K. Srivastava, P. Saikia, & R. K. Mall (Eds.), *Earth Observation in Urban Monitoring* (pp. 171–196). Elsevier. https://doi.org/https://doi.org/10.1016/B978-0-323-99164-3.00003-3

QGIS. (n.d). *OSMDownloader*. Retrieved 25 May 2025 from https://plugins.qgis.org/plugins/OSMDownloader/

Rabby, Y. W., & Li, Y. (2019). An integrated approach to map landslides in Chittagong Hilly Areas, Bangladesh, using Google Earth and field mapping. *Landslides*, *16*(3), 633–645. https://doi.org/10.1007/s10346-018-1107-9

Reiche, J., Mullissa, A., Slagter, B., Gou, Y., Tsendbazar, N.-E., Odongo-Braun, C., Vollrath, A., Weisse, M. J., Stolle, F., & Pickens, A. (2021). Forest disturbance alerts for the Congo Basin using Sentinel-1. *Environmental Research Letters*, *16*(2), 024005.

REMA. (n.d). Landslide Risks Assessment and Mitigation in Four Urban Sub-Catchments in Rwanda. In Rwanda Environment Management Authority (Ed.).

Ruusa, M., Rosser, N. J., & Donoghue, D. N. (2022). Remote sensing for monitoring tropical dryland forests: A review of current research, knowledge gaps and future directions for Southern Africa. *Environmental Research Communications*, *4*(4), 042001.

Samodra, G., Chen, G., Sartohadi, J., & Kasama, K. (2017). Comparing data-driven landslide susceptibility models based on participatory landslide inventory mapping in Purwosari area, Yogyakarta, Java. *Environmental Earth Sciences*, *76*(4), 184. https://doi.org/10.1007/s12665-017-6475-2

Scholte, P., Rugyerinyange, L., Bizimungu, F., Ruzigandekwe, F., Chao, N., Mulindahabi, F., Ntare, N., Babaasa, D., Sheil, D., & Fimbel, R. (2010). Reaching consensus: impact of the liana Sericostachys scandens on forest dynamics in Nyungwe National Park, Rwanda. *Oryx*, *44*(3).

Senyanzobe, J., Mulei, J. M., Bizuru, E., & Nsengimuremyi, C. (2020). Impact of Pteridium aquilinum on vegetation in Nyungwe Forest, Rwanda. *Heliyon*, *6*(9).

Sharma, A., Sajjad, H., Roshani, & Rahaman, M. H. (2024). A systematic review for assessing the impact of climate change on landslides: research gaps and directions for future research. *Spatial Information Research*, *32*(2), 165–185.

Sharma, L., Patel, N., Ghose, M., & Debnath, P. (2014). Application of frequency ratio and likelihood ratio model for geo-spatial modelling of landslide hazard vulnerability assessment and zonation: a case study from the Sikkim Himalayas in India. *Geocarto International*, *29*(2), 128–146.

Silalahi, F. E. S., Arifianti, Y., & Hidayat, F. (2019). Landslide susceptibility assessment using frequency ratio model in Bogor, West Java, Indonesia. *Geoscience Letters*, *6*(1), 1–17.

Sujatha, E. R., & Sridhar, V. (2021). Landslide susceptibility analysis: A logistic regression model case study in Coonoor, India. *Hydrology*, *8*(1), 41.

Sukristiyanti, S., Wikantika, K., Sadisun, I., Yayusman, L., & Telaumbanua, J. (2021). Polygon-based Landslide Inventory for Bandung Basin Using Google Earth. *Indonesian Journal of Geography*, *53*. https://doi.org/10.22146/ijg.58014

Tzouvaras, M., Danezis, C., & Hadjimitsis, D. G. (2020). Small scale landslide detection using Sentinel-1 interferometric SAR coherence. *Remote Sensing*, *12*(10), 1560.

Udahogora, M., Zhaoping, Y., Fang, H., Kayumba, P. M., & Mind'je, R. (2024). Exploring the landscape pattern change analysis for the transboundary Nyungwe-Kibira Forest (2000–2019): a spatially explicit assessment. *Frontiers in Forests and Global Change*, *6*, 1292364.

USGS. (2018). *USGS EROS Archive - Digital Elevation - Shuttle Radar Topography Mission (SRTM) Non-Void Filled*. Retrieved 22 May 2024 from https://www.usgs.gov/centers/eros/science/usgs-eros-archive-digital-elevation-shuttle-radar-topography-mission-srtm-non

Uwihirwe, J. (2021). *Data underlying the research of Integration of observed and model derived groundwater levels in landslide threshold models in Rwanda*. Retrieved 17 November 2024 from https://data.4tu.nl/articles/dataset/Data_underlying_the_research_of_Integration_of_observed_and_model_derived_groundwater_levels_in_landslide_threshold_models_in_Rwanda/15040446

Uwihirwe, J., Hrachowitz, M., & Bogaard, T. (2022). Integration of observed and model-derived groundwater levels in landslide threshold models in Rwanda. *Natural Hazards and Earth System Sciences*, *22*(5), 1723–1742.

Uwihirwe, J., Hrachowitz, M., & Bogaard, T. A. (2020). Landslide precipitation thresholds in Rwanda. *Landslides*, *17*(10), 2469–2481.

Van der Heyden, D. (2016). Carbon Storage and Nutrient Shifts Along an Altitudinal Gradi-ent in Nyungwe Forest, Rwanda. *Faculty of Bioscience Engineering, Ghent University, Belgium*.

Vancutsem, C., Achard, F., Pekel, J.-F., Vieilledent, G., Carboni, S., Simonetti, D., Gallego, J., Aragao, L. E., & Nasi, R. (2021). Long-term (1990–2019) monitoring of forest cover changes in the humid tropics. *Science advances*, *7*(10), eabe1603.

Wang, X., Fan, X., Fang, C., Dai, L., Zhang, W., Zheng, H., & Xu, Q. (2024). Long-term landslide evolution and restoration after the Wenchuan earthquake revealed by time-series remote sensing images. *Geophysical Research Letters*, *51*(2), e2023GL106422.

Wu, Y., Li, W., Wang, Q., Liu, Q., Yang, D., Xing, M., Pei, Y., & Yan, S. (2016). Landslide susceptibility assessment using frequency ratio, statistical index and certainty factor models for the Gangu County, China. *Arabian Journal of Geosciences*, *9*(2), 84.

Xiao, T., & Zhang, L.-M. (2023). Data-driven landslide forecasting: Methods, data completeness, and real-time warning. *Engineering Geology*, *317*, 107068.

Xu, F., Heremans, S., & Somers, B. (2022). Urban land cover mapping with Sentinel-2: A spectro-spatio-temporal analysis. *Urban Informatics*, *1*(1), 8.

Yilmaz, C., Topal, T., & Süzen, M. L. (2012). GIS-based landslide susceptibility mapping using bivariate statistical analysis in Devrek (Zonguldak-Turkey). *Environmental Earth Sciences*, *65*(7), 2161–2178.

Appendix A: Google Earth Image Availability

Table AN-1: Schedule on Google Earth Image Availability in Nyungwe Forest Reserve

Point	2000 - 2004	2005	2006	2007	2008 - 2014	2015	2016	2017	2018	2019	2020	2021	2022	2023	2024
1	**N/A**				**N/A**		30/07/2016	**N/A**				11/03/2021			
1							21/07/2016								
2							28/06/2016					11/03/2021			
2							30/07/2016								
2							21/08/2016								
2							21/09/2016								
3				09/07/2007			28/06/2016		16/08/2018		04/07/2020	11/03/2021	03/03/2022		
3							30/07/2016					19/07/2021	11/07/2022		
3												21/09/2021			
5			07/09/2006	09/07/2007			28/06/2016		16/08/2018		04/07/2020	11/03/2021	03/03/2022		
5												19/07/2021	11/07/2022		
5												21/09/2021			
6			07/09/2006	09/07/2007			28/06/2016		16/08/2018		04/07/2020	11/03/2021	03/03/2022		
6												19/07/2021	11/07/2022		
6												21/09/2021			
9				09/07/2007			28/06/2016				04/07/2020	11/03/2021	03/03/2022		
9												19/07/2021	11/07/2022		
9												21/09/2021			
11				09/07/2007			28/06/2016				04/07/2020	11/03/2021	03/03/2022		
11							21/08/2016								
12				09/07/2007			28/06/2016		11/08/2018	24/08/2019	04/07/2020	11/03/2021	03/03/2022		
12							21/08/2016								
13				09/07/2007			28/06/2016		11/08/2018	24/08/2019	04/07/2020	11/03/2021	03/03/2022		
13							21/08/2016								
15				09/07/2007			28/06/2016		16/08/2018		04/07/2020	11/03/2021	03/03/2022		
15							30/07/2016					19/07/2021	11/07/2022		

Point	2000 - 2004	2005	2006	2007	2008 - 2014	2015	2016	2017	2018	2019	2020	2021	2022	2023	2024
15												21/08/2021			
16				09/07/2007			28/06/2016		16/08/2018		04/07/2020	11/03/2021			
16							30/07/2016					19/07/2021	11/07/2022		
16												21/08/2021			
17				09/07/2007			28/06/2016		16/08/2018		04/07/2020	11/03/2021			
17							30/07/2016					19/07/2021	11/07/2022		
17												21/08/2021			
18				09/07/2007			28/06/2016		16/08/2018		04/07/2020	11/03/2021	03/03/2022		
18							30/07/2016					19/07/2021	11/07/2022		
18												21/08/2021			
19				09/07/2007			28/06/2016		16/08/2018		04/07/2020	11/03/2021	03/03/2022		
19							30/07/2016					19/07/2021	11/07/2022		
19												21/08/2021			
20							30/07/2016				04/07/2020	11/03/2021	03/03/2022		
20							31/07/2016					19/07/2021	11/07/2022		
21							30/07/2016				04/07/2020	11/03/2021	03/03/2022		
21							31/07/2016					19/07/2021	11/07/2022		
22							30/07/2016					11/03/2021	03/03/2022		
22							31/07/2016					19/07/2021	11/07/2022		
23							30/07/2016		16/08/2018		04/07/2020	11/03/2021	03/03/2022		
23							31/07/2016					19/07/2021	11/07/2022		
24							30/07/2016		16/08/2018			11/03/2021	03/03/2022		
24							31/07/2016					19/07/2021	11/07/2022		
25							30/07/2016		11/08/2018			11/03/2021	03/03/2022		
25							31/07/2016		16/08/2018			19/07/2021	11/07/2022		
26							30/07/2016		16/08/2018		04/07/2020	11/03/2021	03/03/2022		
26							31/07/2016					19/07/2021	11/07/2022		
27				09/07/2007			28/06/2016		16/08/2018			11/03/2021	03/03/2022		

Point	2000 - 2004	2005	2006	2007	2008 - 2014	2015	2016	2017	2018	2019	2020	2021	2022	2023	2024
27												19/07/2021	11/07/2022		
27												21/09/2021			
28				09/07/2007			28/06/2016				04/07/2020	11/03/2021	03/03/2022		
28							21/08/2016								
30				09/07/2007			28/06/2016					11/03/2021	03/03/2022		
30							21/08/2016								
31				09/07/2007			28/06/2016						03/03/2022		
							21/08/2016								
32				09/07/2007			28/06/2016					11/03/2021	03/03/2022		
							21/08/2016								
33				09/07/2007			28/06/2016				04/07/2020	11/03/2021	03/03/2022		
							21/08/2016								
34				09/07/2007			28/06/2016		16/08/2016		04/07/2020	11/03/2021	03/03/2022		
												19/07/2021	11/07/2022		
												21/09/2021			
36							31/07/2016			13/08/2019		11/03/2021			
							21/08/2016								
							21/09/2016								
37							31/07/2016		11/08/2018	13/08/2019		11/03/2021	03/03/2022		
							21/08/2016								
							21/09/2016								
39							31/07/2016		11/08/2018	13/08/2019		11/03/2021	03/03/2022		
							21/08/2016								
							21/09/2016								
40							31/07/2016		11/08/2018	13/08/2019		11/03/2021	03/03/2022		
							21/08/2016								
							21/09/2016								
41							31/07/2016		11/08/2018	13/08/2019		11/03/2021	03/03/2022		

Point	2000 - 2004	2005	2006	2007	2008 - 2014	2015	2016	2017	2018	2019	2020	2021	2022	2023	2024
							21/08/2016								
							21/09/2016								
42							31/07/2016		11/08/2018	13/08/2019		11/03/2021	03/03/2022		
							21/08/2016								
							21/09/2016								
43							31/07/2016		11/08/2018	13/08/2019		11/03/2021	03/03/2022		
							21/08/2016								
							21/09/2016								
44							31/07/2016		11/08/2018	13/08/2019		11/03/2021	03/03/2022		
							21/08/2016								
							21/09/2016								
45							31/07/2016		11/08/2018	13/08/2019				03/10/2022	
							21/09/2016			16/08/2019					
46							31/07/2016		11/08/2018	13/08/2019					28/07/2024
							21/09/2016								
47							31/07/2016		11/08/2018	13/08/2019					28/07/2024
							21/09/2016								
48							31/07/2016		11/08/2018	13/08/2019					28/07/2024
							21/09/2016								
49							31/07/2016			13/08/2019					28/07/2024
									11/08/2018						
50							31/07/2016			13/08/2019					28/07/2024
									11/08/2018	16/08/2019					
										18/08/2019					
52							31/07/2016			13/08/2019					28/07/2024
									11/08/2018	16/08/2019					
53							31/07/2016			13/08/2019					28/07/2024
									11/08/2018	16/08/2019					

Point	2000 - 2004	2005	2006	2007	2008 - 2014	2015	2016	2017	2018	2019	2020	2021	2022	2023	2024
54							31/07/2016			13/08/2019					28/07/2024
									11/08/2018	16/08/2019					
55							31/07/2016		11/08/2018	13/08/2019					28/07/2024
										16/08/2019					
										17/08/2019					
56							31/07/2016		11/08/2018	13/08/2019					28/07/2024
										16/08/2019					
57							31/07/2016		11/08/2018	13/08/2019					28/07/2024
										16/08/2019					
58						17/01/2015			01/10/2018	13/08/2019		25/02/2021			28/07/2024
						09/02/2015									
59							31/07/2016			13/08/2019					28/07/2024
									11/08/2018	16/08/2019					
										17/08/2019					
60							31/07/2016			13/08/2019					28/07/2024
									11/08/2018	16/08/2019					
										17/08/2019					
61						09/02/2015	31/07/2016			13/08/2019		25/02/2021		03/10/2022	
							21/09/2016			16/08/2019					
										17/08/2019					
62							31/07/2016			13/08/2019		25/02/2021			
							21/09/2016		11/08/2018	16/08/2019					
										17/08/2019					
63							31/07/2016			13/08/2019		25/02/2021			
							21/09/2016		11/08/2018	16/08/2019					
										17/08/2019					
64							31/07/2016		11/08/2018	13/08/2019				03/10/2022	
							21/09/2016								

Point	2000 - 2004	2005	2006	2007	2008 - 2014	2015	2016	2017	2018	2019	2020	2021	2022	2023	2024
65							31/07/2016		11/08/2018	13/08/2019				03/10/2022	
							21/09/2016								
66							31/07/2016		11/08/2018	13/08/2019				03/10/2022	
							21/09/2016								
67							31/07/2016		11/08/2018	13/08/2019				03/10/2022	
							21/09/2016								
68							31/07/2016		11/08/2018	13/08/2019				03/10/2022	
							21/09/2016								
69							31/07/2016			13/08/2019				03/10/2022	
							21/09/2016		11/08/2018	17/08/2019					
70							31/07/2016		11/08/2018	13/08/2019		11/03/2021		03/10/2022	
							21/09/2016								
71							31/07/2016		11/08/2018	13/08/2019				03/10/2022	
							21/09/2016								
72							31/07/2016		11/08/2018	13/08/2019				03/10/2022	
							21/09/2016								
73							31/07/2016		11/08/2018	13/08/2019		11/03/2021		03/10/2022	
							21/09/2016								
74							31/07/2016		11/08/2018	13/08/2019		11/03/2021		03/10/2022	
							21/09/2016								
75							31/07/2016		11/08/2018	13/08/2019		11/03/2021		03/10/2022	
							21/09/2016								
76									11/08/2018	13/08/2019				03/10/2022	
							21/09/2016								
77							31/07/2016			13/08/2019					
							21/09/2016		11/08/2018	17/08/2019					
78							31/07/2016			13/08/2019					

Point	2000 - 2004	2005	2006	2007	2008 - 2014	2015	2016	2017	2018	2019	2020	2021	2022	2023	2024
							21/09/2016		11/08/2018	17/08/2019					
79							31/07/2016			13/08/2019					
							21/09/2016		11/08/2018	17/08/2019					
80							31/07/2016			13/08/2019					
							21/09/2016		11/08/2018	17/08/2019					
81						09/02/2015	31/07/2016			13/08/2019		25/02/2021		03/10/2022	
							21/09/2016			17/08/2019					
82							31/07/2016			13/08/2019				03/10/2022	
							21/09/2016								
84							31/07/2016			13/08/2019				03/10/2022	
							21/09/2016								
85							31/07/2016			13/08/2019				03/10/2022	
							21/09/2016								
86							31/07/2016			13/08/2019				03/10/2022	
							21/09/2016								
87							31/07/2016			13/08/2019				03/10/2022	
							21/09/2016								
88							31/07/2016			13/08/2019				03/10/2022	
							21/09/2016								
89							31/07/2016			13/08/2019				03/10/2022	
							21/08/2016								
							21/09/2016								
90										13/08/2019				03/10/2022	
							21/08/2016								
							21/09/2016								
91										13/08/2019				03/10/2022	
							21/08/2016								

Point	**2000 - 2004**	**2005**	**2006**	**2007**	**2008 - 2014**	**2015**	**2016**	**2017**	**2018**	**2019**	**2020**	**2021**	**2022**	**2023**	**2024**
							21/09/2016								
92										13/08/2019				03/10/2022	
							21/08/2016								
93							21/08/2016			13/08/2019				03/10/2022	
94						09/02/2015	21/09/2016			13/08/2019				03/10/2022	
						29/02/2015				17/08/2019					
95							21/08/2016			13/08/2019		11/03/2021		03/10/2022	
96							21/08/2016			13/08/2019		11/03/2021		03/10/2022	
97							21/08/2016			13/08/2019		11/03/2021		03/10/2022	
98							21/08/2016			13/08/2019		11/03/2021		03/10/2022	
100							21/08/2016			13/08/2019		11/03/2021			
										24/08/2019		05/07/2021			
												19/07/2021			
101							21/08/2016			13/08/2019		11/03/2021			
										24/08/2019		05/07/2021			
												19/07/2021			
102							21/08/2016			13/08/2019		11/03/2021			
										24/08/2019		05/07/2021			
												19/07/2021			
103							21/08/2016			13/08/2019		11/03/2021			
										24/08/2019		05/07/2021			
												19/07/2021			
106							21/08/2016			13/08/2019		11/03/2021			
										24/08/2019		05/07/2021			
												19/07/2021			
107							21/08/2016			13/08/2019		19/07/2021		03/10/2022	
										24/08/2019					

Point	2000 - 2004	2005	2006	2007	2008 - 2014	2015	2016	2017	2018	2019	2020	2021	2022	2023	2024
108							21/08/2016			13/08/2019				03/10/2022	
109							21/08/2016			13/08/2019				03/10/2022	
110							21/08/2016			13/08/2019				03/10/2022	
111							21/08/2016			13/08/2019				03/10/2022	
112							21/08/2016			13/08/2019				03/10/2022	
113							21/08/2016			13/08/2019				03/10/2022	
114							21/08/2016			13/08/2019				03/10/2022	
115							21/08/2016			13/08/2019				03/10/2022	
116						29/08/2015	21/08/2016			13/08/2019				03/10/2022	
124						29/08/2015	21/08/2016			13/08/2019		19/07/2021		03/10/2022	19/06/2024
125		28/06/2005				29/08/2015	21/08/2016			13/08/2019		19/07/2021		03/10/2022	
125		03/07/2005													
126		28/06/2005				29/08/2015						19/07/2021			19/06/2024
126		03/07/2005													
127		28/06/2005				29/08/2015						19/07/2021			19/06/2024
127		03/07/2005													

Appendix B: Estimation of Missed Landslides

1. **Years with usable imagery**

Total = **107 landslides**

Average = **11.9 per year.**

However, this this is skewed by extreme years (2021 and 2023).

2. **Removing outliers**

Outliers: 2021 (33) and 2023 (34) distort the estimate.

Remaining years: 2015, 2016, 2018, 2019, 2020, 2022, 2024

Landslides = 2 + 13 + 4 + 6 + 3 + 1 + 11 = **40** Years = 7

Annual rate = 40 / 7 = ~5.7 landslides per year

3. **Years with no usable imagery**

Years with **no imagery**:

- 2000–2004 = 5 years
- 2008–2014 = 7 years
- 2017 = 1 year
- Total = 13 years

4. **Estimate missed landslides**

Estimated number of landslides = 13×5.7= ~74**.1**

Appendix C: Backward Logistic Regression

Case Processing Summary			
Unweighted Cases[a]		N	Percent
Selected Cases	Included in Analysis	214	100.0
	Missing Cases	0	.0
	Total	214	100.0
Unselected Cases		0	.0
Total		214	100.0

a. If weight is in effect, see classification table for the total number of cases.

Dependent Variable Encoding	
Original Value	Internal Value
0	0
1	1

Categorical Variables Codings							
			Parameter coding				
		Frequency	(1)	(2)	(3)	(4)	(5)
Aspect_Direction	North	27	.000	.000	.000	.000	.000
	NE	29	1.000	.000	.000	.000	.000
	East	31	.000	1.000	.000	.000	.000
	SE	25	.000	.000	1.000	.000	.000
	South	42	.000	.000	.000	1.000	.000
	SW	22	.000	.000	.000	.000	1.000
	West	18	.000	.000	.000	.000	.000
	NW	20	.000	.000	.000	.000	.000
North_Exposure	0	139	.000				
	1	75	1.000				
East_Exposure	0	181	.000				
	1	33	1.000				

Categorical Variables Codings	
	Parameter coding

		(6)	(7)
Aspect_Direction	North	.000	.000
	NE	.000	.000
	East	.000	.000
	SE	.000	.000
	South	.000	.000
	SW	.000	.000
	West	1.000	.000
	NW	.000	1.000
North_Exposure	0		
	1		
East_Exposure	0		
	1		

Block 0: Beginning Block

Classification Table[a,b]					
			Predicted		
			Landslide		
	Observed		0	1	Percentage Correct
Step 0	Landslide	0	0	107	.0
		1	0	107	100.0
	Overall Percentage				50.0
a. Constant is included in the model.					
b. The cut value is .500					

Variables in the Equation							
		B	S.E.	Wald	df	Sig.	Exp(B)
Step 0	Constant	.000	.137	.000	1	1.000	1.000

Variables not in the Equation					
			Score	df	Sig.
Step 0	Variables	Zscore(Elevation)	.058	1	.809
		Zscore(Rainfall)	15.655	1	<.001
		Zscore(WI)	2.469	1	.116

		Zscore(Slope)	18.833	1	<.001
		Zscore(SPI)	1.019	1	.313
		Zscore(Shifted_Dist_to_Roads)	26.136	1	<.001
		Zscore(Shifted_Dist_to_Rivers)	.976	1	.323
		Zscore(Shifted_Prof_Curvature_0.012)	3.471	1	.062
		Zscore(Shifted_Plan_Curvature_0.07)	.008	1	.929
		East_Exposure(1)	4.335	1	.037
		North_Exposure(1)	1.006	1	.316
		Aspect_Direction	6.800	7	.450
		Aspect_Direction(1)	.040	1	.842
		Aspect_Direction(2)	3.056	1	.080
		Aspect_Direction(3)	.408	1	.523
		Aspect_Direction(4)	.000	1	1.000
		Aspect_Direction(5)	.000	1	1.000
		Aspect_Direction(6)	3.882	1	.049
		Aspect_Direction(7)	.221	1	.639
	Overall Statistics		64.511	18	<.001

Block 1: Method = Backward Stepwise (Likelihood Ratio)

Omnibus Tests of Model Coefficients

		Chi-square	df	Sig.
Step 1	Step	75.502	18	<.001
	Block	75.502	18	<.001
	Model	75.502	18	<.001
Step 2[a]	Step	-.018	1	.892
	Block	75.484	17	<.001
	Model	75.484	11	<.001
Step 3[a]	Step	-.039	1	.843
	Block	75.444	16	<.001
	Model	75.444	10	<.001
Step 4[a]	Step	-5.179	7	.638
	Block	70.266	9	<.001
	Model	70.266	9	<.001
Step 5[a]	Step	-.727	1	.394
	Block	69.539	8	<.001

	Model	69.539	8	<.001
Step 6[a]	Step	-1.429	1	.232
	Block	68.111	7	<.001
	Model	68.111	7	<.001
Step 7[a]	Step	-1.537	1	.215
	Block	66.574	6	<.001
	Model	66.574	6	<.001

a. A negative Chi-squares value indicates that the Chi-squares value has decreased from the previous step.

Model Summary

Step	-2 Log likelihood	Cox & Snell R Square	Nagelkerke R Square
1	221.165[a]	.297	.396
2	221.183[a]	.297	.396
3	221.223[a]	.297	.396
4	226.401[a]	.280	.373
5	227.128[b]	.277	.370
6	228.556[b]	.273	.363
7	230.093[b]	.267	.356

a. Estimation terminated at iteration number 7 because parameter estimates changed by less than .001.

b. Estimation terminated at iteration number 5 because parameter estimates changed by less than .001.

Hosmer and Lemeshow Test

Step	Chi-square	df	Sig.
1	1.715	8	.989
2	2.308	8	.970
3	3.989	8	.858
4	4.342	8	.825
5	8.576	8	.379
6	6.584	8	.582
7	2.733	8	.950

Contingency Table for Hosmer and Lemeshow Test						
		Landslide = 0		Landslide = 1		Total
		Observed	Expected	Observed	Expected	
Step 1	1	20	20.031	1	.969	21
	2	18	18.273	3	2.727	21
	3	15	15.500	6	5.500	21
	4	14	12.996	7	8.004	21
	5	12	11.486	9	9.514	21
	6	10	9.523	11	11.477	21
	7	6	6.977	15	14.023	21
	8	5	5.472	16	15.528	21
	9	3	4.057	18	16.943	21
	10	4	2.685	21	22.315	25
Step 2	1	20	20.021	1	.979	21
	2	18	18.283	3	2.717	21
	3	15	15.489	6	5.511	21
	4	15	12.998	6	8.002	21
	5	11	11.505	10	9.495	21
	6	10	9.527	11	11.473	21
	7	6	6.963	15	14.037	21
	8	5	5.472	16	15.528	21
	9	3	4.054	18	16.946	21
	10	4	2.687	21	22.313	25
Step 3	1	21	20.021	0	.979	21
	2	17	18.271	4	2.729	21
	3	15	15.487	6	5.513	21
	4	15	13.028	6	7.972	21
	5	11	11.478	10	9.522	21
	6	10	9.513	11	11.487	21
	7	6	7.005	15	13.995	21
	8	5	5.459	16	15.541	21
	9	3	4.063	18	16.937	21
	10	4	2.675	21	22.325	25
Step 4	1	20	19.787	1	1.213	21
	2	19	17.644	2	3.356	21
	3	14	15.482	7	5.518	21
	4	13	13.420	8	7.580	21
	5	13	11.308	8	9.692	21
	6	7	9.263	14	11.737	21
	7	7	7.272	14	13.728	21

	8	7	5.634	14	15.366	21
	9	3	4.353	18	16.647	21
	10	4	2.838	21	22.162	25
Step 5	1	20	19.702	1	1.298	21
	2	18	17.582	3	3.418	21
	3	14	15.441	7	5.559	21
	4	15	13.498	6	7.502	21
	5	13	11.386	8	9.614	21
	6	7	9.267	14	11.733	21
	7	4	7.273	17	13.727	21
	8	9	5.681	12	15.319	21
	9	3	4.337	18	16.663	21
	10	4	2.833	21	22.167	25
Step 6	1	21	19.614	0	1.386	21
	2	17	17.491	4	3.509	21
	3	14	15.443	7	5.557	21
	4	14	13.386	7	7.614	21
	5	13	11.502	8	9.498	21
	6	5	9.187	16	11.813	21
	7	8	7.414	13	13.586	21
	8	7	5.639	14	15.361	21
	9	5	4.483	16	16.517	21
	10	3	2.840	22	22.160	25
Step 7	1	20	19.613	1	1.387	21
	2	18	17.592	3	3.408	21
	3	15	15.127	6	5.873	21
	4	12	13.194	9	7.806	21
	5	13	11.168	8	9.832	21
	6	7	9.445	14	11.555	21
	7	7	7.620	14	13.380	21
	8	7	5.824	14	15.176	21
	9	5	4.545	16	16.455	21
	10	3	2.872	22	22.128	25

Classification Table[a]

			Predicted		
			Landslide		Percentage Correct
	Observed		0	1	
Step 1	Landslide	0	79	28	73.8

		1	26	81	75.7
	Overall Percentage				74.8
Step 2	Landslide	0	79	28	73.8
		1	27	80	74.8
	Overall Percentage				74.3
Step 3	Landslide	0	79	28	73.8
		1	27	80	74.8
	Overall Percentage				74.3
Step 4	Landslide	0	79	28	73.8
		1	24	83	77.6
	Overall Percentage				75.7
Step 5	Landslide	0	79	28	73.8
		1	24	83	77.6
	Overall Percentage				75.7
Step 6	Landslide	0	79	28	73.8
		1	25	82	76.6
	Overall Percentage				75.2
Step 7	Landslide	0	76	31	71.0
		1	27	80	74.8
	Overall Percentage				72.9

a. The cut value is .500

Variables in the Equation

		B	S.E.	Wald	df	Sig.	Exp(B)	95% C.I.for EXP(B)	
								Lower	Upper
Step 1[a]	Zscore(Elevation)	.263	.172	2.354	1	.125	1.301	.929	1.822
	Zscore(Rainfall)	-.507	.191	7.060	1	.008	.602	.414	.875
	Zscore(WI)	-.033	.226	.021	1	.885	.968	.621	1.508
	Zscore(Slope)	.802	.215	13.938	1	<.001	2.229	1.463	3.396
	Zscore(SPI)	-.255	.704	.131	1	.718	.775	.195	3.083
	Zscore(Shifted_Dist_to_Roads)	-.799	.226	12.472	1	<.001	.450	.289	.701
	Zscore(Shifted_Dist_to_Rivers)	.184	.176	1.094	1	.296	1.202	.851	1.697
	Zscore(Shifted_Prof_Curvature_0.012)	-.527	.198	7.059	1	.008	.590	.400	.871

	Zscore(Shifted_Plan_Curvature_0.07)	.025	.186	.018	1	.892	1.025	.712	1.476
	East_Exposure(1)	.612	1.176	.271	1	.603	1.844	.184	18.489
	North_Exposure(1)	-.941	.921	1.043	1	.307	.390	.064	2.374
	Aspect_Direction			4.805	7	.684			
	Aspect_Direction(1)	.161	.661	.060	1	.807	1.175	.322	4.289
	Aspect_Direction(2)	-.275	1.267	.047	1	.828	.759	.063	9.091
	Aspect_Direction(3)	.152	1.108	.019	1	.891	1.164	.133	10.218
	Aspect_Direction(4)	-.627	1.071	.343	1	.558	.534	.066	4.357
	Aspect_Direction(5)	.028	1.124	.001	1	.980	1.029	.114	9.313
	Aspect_Direction(6)	-1.259	1.111	1.284	1	.257	.284	.032	2.507
	Aspect_Direction(7)	.188	.750	.063	1	.802	1.207	.277	5.251
	Constant	.364	1.018	.128	1	.720	1.440		
Step 2[a]	Zscore(Elevation)	.264	.172	2.350	1	.125	1.302	.929	1.823
	Zscore(Rainfall)	-.509	.191	7.123	1	.008	.601	.414	.874
	Zscore(WI)	-.043	.215	.039	1	.843	.958	.629	1.459
	Zscore(Slope)	.801	.215	13.913	1	<.001	2.227	1.462	3.391
	Zscore(SPI)	-.250	.699	.128	1	.721	.779	.198	3.067
	Zscore(Shifted_Dist_to_Roads)	-.797	.226	12.459	1	<.001	.451	.289	.702
	Zscore(Shifted_Dist_to_Rivers)	.185	.176	1.109	1	.292	1.203	.853	1.699
	Zscore(Shifted_Prof_Curvature_0.012)	-.525	.198	7.050	1	.008	.592	.402	.872
	East_Exposure(1)	.611	1.174	.271	1	.603	1.843	.185	18.395
	North_Exposure(1)	-.932	.922	1.024	1	.312	.394	.065	2.396
	Aspect_Direction			4.791	7	.685			
	Aspect_Direction(1)	.159	.660	.058	1	.809	1.173	.321	4.279
	Aspect_Direction(2)	-.271	1.266	.046	1	.830	.762	.064	9.119
	Aspect_Direction(3)	.152	1.110	.019	1	.891	1.165	.132	10.262
	Aspect_Direction(4)	-.623	1.072	.338	1	.561	.536	.066	4.386
	Aspect_Direction(5)	.033	1.126	.001	1	.976	1.034	.114	9.396
	Aspect_Direction(6)	-1.250	1.111	1.267	1	.260	.286	.032	2.526
	Aspect_Direction(7)	.186	.750	.061	1	.804	1.204	.277	5.235
	Constant	.360	1.019	.125	1	.724	1.433		
Step 3[a]	Zscore(Elevation)	.264	.172	2.347	1	.126	1.302	.929	1.824
	Zscore(Rainfall)	-.509	.191	7.112	1	.008	.601	.413	.874
	Zscore(Slope)	.820	.191	18.455	1	<.001	2.271	1.562	3.302
	Zscore(SPI)	-.273	.748	.133	1	.715	.761	.176	3.295
	Zscore(Shifted_Dist_to_Roads)	-.794	.225	12.437	1	<.001	.452	.291	.703
	Zscore(Shifted_Dist_to_Rivers)	.185	.176	1.108	1	.293	1.203	.853	1.698

	Zscore(Shifted_Prof_Curvature_0.012)	-.513	.189	7.404	1	.007	.599	.414	.866
	East_Exposure(1)	.592	1.170	.256	1	.613	1.807	.182	17.909
	North_Exposure(1)	-.946	.918	1.060	1	.303	.388	.064	2.350
	Aspect_Direction			4.879	7	.675			
	Aspect_Direction(1)	.154	.661	.055	1	.815	1.167	.320	4.261
	Aspect_Direction(2)	-.262	1.269	.043	1	.837	.770	.064	9.261
	Aspect_Direction(3)	.152	1.111	.019	1	.891	1.164	.132	10.262
	Aspect_Direction(4)	-.640	1.068	.359	1	.549	.527	.065	4.278
	Aspect_Direction(5)	.025	1.124	.000	1	.983	1.025	.113	9.283
	Aspect_Direction(6)	-1.258	1.111	1.283	1	.257	.284	.032	2.507
	Aspect_Direction(7)	.183	.750	.059	1	.808	1.200	.276	5.222
	Constant	.372	1.018	.133	1	.715	1.450		
Step 4[a]	Zscore(Elevation)	.294	.168	3.056	1	.080	1.342	.965	1.866
	Zscore(Rainfall)	-.491	.186	6.987	1	.008	.612	.425	.881
	Zscore(Slope)	.781	.178	19.173	1	<.001	2.184	1.540	3.098
	Zscore(SPI)	-.302	.863	.123	1	.726	.739	.136	4.011
	Zscore(Shifted_Dist_to_Roads)	-.753	.216	12.189	1	<.001	.471	.309	.719
	Zscore(Shifted_Dist_to_Rivers)	.190	.171	1.239	1	.266	1.210	.865	1.691
	Zscore(Shifted_Prof_Curvature_0.012)	-.524	.179	8.551	1	.003	.592	.417	.841
	East_Exposure(1)	.749	.494	2.295	1	.130	2.115	.803	5.574
	North_Exposure(1)	-.515	.373	1.900	1	.168	.598	.288	1.243
	Constant	.002	.246	.000	1	.994	1.002		
Step 5[a]	Zscore(Elevation)	.297	.168	3.117	1	.077	1.346	.968	1.873
	Zscore(Rainfall)	-.499	.186	7.191	1	.007	.607	.422	.874
	Zscore(Slope)	.791	.178	19.698	1	<.001	2.205	1.555	3.127
	Zscore(Shifted_Dist_to_Roads)	-.753	.216	12.119	1	<.001	.471	.308	.720
	Zscore(Shifted_Dist_to_Rivers)	.203	.170	1.424	1	.233	1.225	.878	1.710
	Zscore(Shifted_Prof_Curvature_0.012)	-.506	.177	8.139	1	.004	.603	.426	.854
	East_Exposure(1)	.738	.494	2.230	1	.135	2.092	.794	5.512
	North_Exposure(1)	-.547	.371	2.172	1	.141	.578	.279	1.198
	Constant	.027	.237	.013	1	.909	1.027		
Step 6[a]	Zscore(Elevation)	.292	.169	2.994	1	.084	1.340	.962	1.865
	Zscore(Rainfall)	-.472	.183	6.683	1	.010	.624	.436	.892
	Zscore(Slope)	.815	.178	20.938	1	<.001	2.258	1.593	3.201
	Zscore(Shifted_Dist_to_Roads)	-.748	.212	12.508	1	<.001	.473	.313	.716
	Zscore(Shifted_Prof_Curvature_0.012)	-.481	.174	7.625	1	.006	.618	.439	.870
	East_Exposure(1)	.801	.486	2.719	1	.099	2.227	.860	5.767

	North_Exposure(1)	-.444	.360	1.521	1	.217	.642	.317	1.299
	Constant	-.011	.235	.002	1	.961	.989		
Step 7[a]	Zscore(Elevation)	.289	.169	2.924	1	.087	1.335	.959	1.859
	Zscore(Rainfall)	-.450	.180	6.242	1	.012	.638	.448	.908
	Zscore(Slope)	.803	.178	20.243	1	<.001	2.232	1.573	3.166
	Zscore(Shifted_Dist_to_Roads)	-.758	.213	12.691	1	<.001	.468	.309	.711
	Zscore(Shifted_Prof_Curvature_0.012)	-.462	.173	7.137	1	.008	.630	.449	.884
	East_Exposure(1)	.984	.462	4.544	1	.033	2.676	1.083	6.615
	Constant	-.199	.180	1.224	1	.269	.820		

a. Variable(s) entered on step 1: Zscore(Elevation), Zscore(Rainfall), Zscore(WI), Zscore(Slope), Zscore(SPI), Zscore(Shifted_Dist_to_Roads), Zscore(Shifted_Dist_to_Rivers), Zscore(Shifted_Prof_Curvature_0.012), Zscore(Shifted_Plan_Curvature_0.07), East_Exposure, North_Exposure, Aspect_Direction.

Model if Term Removed

Variable		Model Log Likelihood	Change in -2 Log Likelihood	df	Sig. of the Change
Step 1	Zscore(Elevation)	-111.773	2.382	1	.123
	Zscore(Rainfall)	-114.313	7.461	1	.006
	Zscore(WI)	-110.593	.021	1	.885
	Zscore(Slope)	-118.450	15.735	1	<.001
	Zscore(SPI)	-110.828	.491	1	.483
	Zscore(Shifted_Dist_to_Roads)	-118.579	15.993	1	<.001
	Zscore(Shifted_Dist_to_Rivers)	-111.130	1.096	1	.295
	Zscore(Shifted_Prof_Curvature_0.012)	-114.300	7.435	1	.006
	Zscore(Shifted_Plan_Curvature_0.07)	-110.592	.018	1	.892
	East_Exposure	-110.723	.282	1	.596
	North_Exposure	-111.124	1.083	1	.298
	Aspect_Direction	-113.133	5.101	7	.648
Step 2	Zscore(Elevation)	-111.781	2.379	1	.123
	Zscore(Rainfall)	-114.365	7.546	1	.006
	Zscore(WI)	-110.611	.039	1	.843
	Zscore(Slope)	-118.453	15.724	1	<.001
	Zscore(SPI)	-110.829	.475	1	.491
	Zscore(Shifted_Dist_to_Roads)	-118.589	15.995	1	<.001
	Zscore(Shifted_Dist_to_Rivers)	-111.147	1.110	1	.292
	Zscore(Shifted_Prof_Curvature_0.012)	-114.308	7.433	1	.006
	East_Exposure	-110.732	.282	1	.596
	North_Exposure	-111.125	1.066	1	.302

	Aspect_Direction	-113.134	5.084	7	.650
Step 3	Zscore(Elevation)	-111.799	2.376	1	.123
	Zscore(Rainfall)	-114.378	7.533	1	.006
	Zscore(Slope)	-121.260	21.298	1	<.001
	Zscore(SPI)	-110.921	.619	1	.431
	Zscore(Shifted_Dist_to_Roads)	-118.601	15.979	1	<.001
	Zscore(Shifted_Dist_to_Rivers)	-111.166	1.109	1	.292
	Zscore(Shifted_Prof_Curvature_0.012)	-114.536	7.849	1	.005
	East_Exposure	-110.744	.266	1	.606
	North_Exposure	-111.164	1.105	1	.293
	Aspect_Direction	-113.201	5.179	7	.638
Step 4	Zscore(Elevation)	-114.763	3.125	1	.077
	Zscore(Rainfall)	-116.884	7.366	1	.007
	Zscore(Slope)	-124.277	22.152	1	<.001
	Zscore(SPI)	-113.564	.727	1	.394
	Zscore(Shifted_Dist_to_Roads)	-120.849	15.297	1	<.001
	Zscore(Shifted_Dist_to_Rivers)	-113.821	1.242	1	.265
	Zscore(Shifted_Prof_Curvature_0.012)	-117.721	9.041	1	.003
	East_Exposure	-114.379	2.357	1	.125
	North_Exposure	-114.163	1.925	1	.165
Step 5	Zscore(Elevation)	-115.159	3.189	1	.074
	Zscore(Rainfall)	-117.358	7.587	1	.006
	Zscore(Slope)	-125.136	23.144	1	<.001
	Zscore(Shifted_Dist_to_Roads)	-121.178	15.229	1	<.001
	Zscore(Shifted_Dist_to_Rivers)	-114.278	1.429	1	.232
	Zscore(Shifted_Prof_Curvature_0.012)	-117.846	8.565	1	.003
	East_Exposure	-114.708	2.288	1	.130
	North_Exposure	-114.666	2.203	1	.138
Step 6	Zscore(Elevation)	-115.809	3.062	1	.080
	Zscore(Rainfall)	-117.779	7.002	1	.008
	Zscore(Slope)	-126.649	24.741	1	<.001
	Zscore(Shifted_Dist_to_Roads)	-122.107	15.657	1	<.001
	Zscore(Shifted_Prof_Curvature_0.012)	-118.280	8.004	1	.005
	East_Exposure	-115.683	2.809	1	.094
	North_Exposure	-115.047	1.537	1	.215
Step 7	Zscore(Elevation)	-116.542	2.990	1	.084
	Zscore(Rainfall)	-118.294	6.495	1	.011
	Zscore(Slope)	-127.019	23.944	1	<.001
	Zscore(Shifted_Dist_to_Roads)	-123.022	15.950	1	<.001
	Zscore(Shifted_Prof_Curvature_0.012)	-118.781	7.469	1	.006

	East_Exposure	-117.435	4.777	1	.029

Variables not in the Equation					
			Score	df	Sig.
Step 2[a]	Variables	Zscore(Shifted_Plan_Curvature_0.07)	.018	1	.892
	Overall Statistics		.018	1	.892
Step 3[b]	Variables	Zscore(WI)	.039	1	.843
		Zscore(Shifted_Plan_Curvature_0.07)	.037	1	.848
	Overall Statistics		.057	2	.972
Step 4[c]	Variables	Zscore(WI)	.134	1	.714
		Zscore(Shifted_Plan_Curvature_0.07)	.006	1	.937
		Aspect_Direction	5.049	7	.654
		Aspect_Direction(1)	.124	1	.724
		Aspect_Direction(2)	.063	1	.802
		Aspect_Direction(3)	1.610	1	.204
		Aspect_Direction(4)	.942	1	.332
		Aspect_Direction(5)	.668	1	.414
		Aspect_Direction(6)	2.711	1	.100
		Aspect_Direction(7)	.127	1	.722
	Overall Statistics		5.102	9	.825
Step 5[d]	Variables	Zscore(WI)	.367	1	.545
		Zscore(SPI)	.475	1	.491
		Zscore(Shifted_Plan_Curvature_0.07)	.002	1	.967
		Aspect_Direction	5.153	7	.641
		Aspect_Direction(1)	.186	1	.666
		Aspect_Direction(2)	.062	1	.804
		Aspect_Direction(3)	1.648	1	.199
		Aspect_Direction(4)	.949	1	.330
		Aspect_Direction(5)	.658	1	.417
		Aspect_Direction(6)	2.705	1	.100
		Aspect_Direction(7)	.166	1	.684
	Overall Statistics		5.602	10	.848
Step 6[e]	Variables	Zscore(WI)	.430	1	.512
		Zscore(SPI)	.616	1	.433
		Zscore(Shifted_Dist_to_Rivers)	1.435	1	.231
		Zscore(Shifted_Plan_Curvature_0.07)	.008	1	.930
		Aspect_Direction	5.312	7	.622
		Aspect_Direction(1)	.154	1	.695
		Aspect_Direction(2)	.033	1	.855

		Aspect_Direction(3)	1.862	1	.172
		Aspect_Direction(4)	.887	1	.346
		Aspect_Direction(5)	.524	1	.469
		Aspect_Direction(6)	2.938	1	.087
		Aspect_Direction(7)	.145	1	.703
	Overall Statistics		7.060	11	.794
Step 7[f]	Variables	Zscore(WI)	.636	1	.425
		Zscore(SPI)	.783	1	.376
		Zscore(Shifted_Dist_to_Rivers)	.765	1	.382
		Zscore(Shifted_Plan_Curvature_0.07)	.000	1	1.000
		North_Exposure(1)	1.530	1	.216
		Aspect_Direction	5.995	7	.540
		Aspect_Direction(1)	.070	1	.792
		Aspect_Direction(2)	.031	1	.860
		Aspect_Direction(3)	2.918	1	.088
		Aspect_Direction(4)	.084	1	.771
		Aspect_Direction(5)	1.097	1	.295
		Aspect_Direction(6)	2.142	1	.143
		Aspect_Direction(7)	.004	1	.948
	Overall Statistics		8.568	12	.739

a. Variable(s) removed on step 2: Zscore(Shifted_Plan_Curvature_0.07).

b. Variable(s) removed on step 3: Zscore(WI).

c. Variable(s) removed on step 4: Aspect_Direction.

d. Variable(s) removed on step 5: Zscore(SPI).

e. Variable(s) removed on step 6: Zscore(Shifted_Dist_to_Rivers).

f. Variable(s) removed on step 7: North_Exposure.

Appendix D: TMF Detected Landslides

Name	Area (m^2)	2000	2001	2002	2003	2004	2005	2006	2007	2008	2009	2010	2011	2012	2013	2014	2015	2016	2017	2018	2019	2020	2021	2022	2023	2024
1	3991.5	1	1	1	1	1	1	1	1	1	1	1	1	1	1	1	2	2	2	2	2	2	2	2	2	2
6	591.0	1	1	1	1	1	1	1	1	1	1	1	1	1	1	1	1	1	1	1	1	3	3	3	3	3
12	14531.6	2	2	2	2	2	2	2	2	2	2	2	2	2	2	2	2	2	3	3	3	3	3	3	3	3
15	251.4	1	1	1	1	1	1	1	1	1	1	1	1	1	1	1	1	1	1	1	1	1	2	2	2	2
17	236.9	1	1	1	1	1	1	1	1	1	1	1	1	1	1	1	1	1	1	1	1	1	2	2	2	2
18	162.3	1	1	1	1	1	1	1	1	1	1	1	1	1	1	1	1	1	1	1	1	1	2	2	2	2
19	1553.6	1	1	1	1	1	1	1	1	1	1	1	1	1	1	1	1	1	1	1	1	1	2	2	2	2
20	222.4	1	1	1	1	1	1	1	1	1	1	1	1	1	1	1	1	1	1	1	1	1	2	2	2	2
21	489.3	1	1	1	1	1	1	1	1	1	1	1	1	1	1	1	1	1	1	1	1	1	2	2	2	2
28	674.1	1	1	1	1	1	1	1	1	1	1	1	1	1	1	1	1	1	1	1	1	2	2	2	2	2
30	1168.0	1	1	1	1	1	1	1	1	1	1	1	1	1	1	1	1	1	1	1	1	2	2	2	2	2
31	2640.5	1	1	1	1	1	1	1	1	1	1	1	1	1	1	1	1	1	2	2	2	2	2	2	2	2
32	2214.7	1	1	1	1	1	1	1	1	1	1	1	1	1	1	1	1	1	2	2	2	2	2	2	2	2
33	1665.0	1	1	1	1	1	1	1	1	1	1	1	1	1	1	3	3	3	3	3	3	3	3	3	3	4
34	1623.1	1	1	1	1	1	1	1	1	1	1	1	1	1	1	1	1	3	3	3	3	3	3	3	3	3
37	3229.7	1	1	1	1	1	1	1	1	1	1	1	1	1	1	1	1	2	2	2	2	2	2	2	2	2
40	605.1	1	1	1	1	1	1	1	1	1	1	1	1	1	1	1	1	1	1	1	1	1	1	3	3	3
42	1419.2	1	1	1	1	1	1	1	1	1	1	1	1	1	1	1	1	1	1	1	1	2	2	2	2	2
43	698.2	1	1	1	3	3	3	3	3	3	3	3	3	3	3	3	3	3	3	4	4	4	4	4	4	3
44	11207.2	1	1	1	1	1	1	1	1	1	1	1	1	1	1	1	1	1	1	1	1	1	2	2	2	2
47	165.9	1	1	1	1	1	1	1	1	1	1	1	1	1	1	1	1	1	1	1	1	1	2	2	2	2
49	2879.9	1	1	1	1	1	1	1	1	1	1	1	1	1	1	1	1	1	1	1	1	1	1	1	1	3
50	1768.3	1	1	1	1	1	1	1	1	1	1	1	1	1	1	1	1	1	1	1	1	1	1	1	1	2
52	644.5	1	1	1	1	1	1	1	1	1	1	1	1	1	1	1	1	1	1	1	1	1	1	1	2	2
53	370.2	1	1	1	1	1	1	1	1	1	1	1	1	1	1	1	1	1	1	1	1	2	2	2	2	2
54	185.1	1	1	1	1	1	1	1	1	1	1	1	1	1	1	1	1	1	1	1	1	1	1	1	1	2

Name	Area (m^2)	2000	2001	2002	2003	2004	2005	2006	2007	2008	2009	2010	2011	2012	2013	2014	2015	2016	2017	2018	2019	2020	2021	2022	2023	2024
62	4442.9	1	1	1	1	1	1	1	1	1	1	1	1	1	1	1	1	1	1	1	1	1	2	2	2	2
63	1189.0	1	1	1	1	1	1	1	1	1	1	1	1	1	1	1	1	1	1	1	1	2	2	2	2	2
64	2087.0	1	1	1	1	1	1	1	1	1	1	1	1	1	1	1	1	1	1	2	2	2	2	2	2	2
66	1357.8	1	1	1	1	1	1	1	1	1	1	1	1	1	1	1	1	1	1	1	1	1	1	1	2	2
69	3094.2	1	1	1	1	1	1	1	1	1	1	1	1	1	1	1	1	1	1	1	1	1	1	1	2	2
70	1615.7	1	1	1	1	1	1	1	1	1	1	2	2	2	2	2	2	2	2	2	2	2	2	2	3	2
71	7907.6	1	1	1	1	1	1	1	1	1	1	1	1	1	1	1	1	1	1	1	1	1	1	1	2	2
72	1296.2	1	1	1	1	1	1	1	1	1	1	1	1	1	1	1	1	1	1	1	1	1	1	1	3	2
73	785.9	1	1	1	1	1	1	1	1	1	1	1	1	1	1	1	1	1	1	1	1	1	1	1	2	2
77	7535.3	1	1	1	1	1	1	1	1	1	1	1	1	1	1	1	1	1	1	1	1	1	1	1	3	2
78	2988.7	1	1	1	1	1	1	1	1	1	1	1	1	1	1	1	1	1	1	1	1	1	1	1	2	2
81	2877.3	1	1	1	1	1	1	1	1	1	1	1	1	1	1	1	1	1	1	1	1	1	1	1	2	2
84	896.6	1	1	1	1	1	1	1	1	1	1	1	1	1	1	1	1	1	1	1	1	1	1	1	1	2
88	3804.1	1	1	1	1	1	1	1	1	1	1	1	1	1	1	1	1	1	1	1	1	1	1	1	2	2
89	1569.0	1	1	1	1	1	1	1	1	1	1	1	1	1	1	1	1	1	1	1	1	1	3	3	3	2
90	1645.7	1	1	1	1	1	1	1	1	1	1	1	1	1	1	1	1	1	1	1	1	2	2	2	2	2
91	263.5	1	1	1	1	1	1	1	1	1	1	1	1	1	1	1	1	1	1	1	1	1	1	1	2	3
92	2034.7	1	1	1	1	1	1	1	1	1	1	1	1	1	1	1	1	1	1	1	1	1	1	1	1	3
93	1489.1	1	1	1	1	1	1	1	1	1	1	1	1	1	1	1	1	1	1	1	1	2	2	2	2	2
94	5415.2	1	1	1	1	1	1	1	1	1	1	1	1	1	1	1	1	1	1	1	1	1	1	1	3	3
98	11899.7	1	1	1	1	1	1	1	1	1	1	1	1	1	1	1	1	3	3	3	3	3	4	4	4	4
100	920.4	1	1	1	1	1	1	1	1	1	1	1	1	1	1	1	1	1	1	1	1	2	2	2	2	2
110	5203.3	1	1	1	1	1	1	1	1	1	1	1	1	1	1	1	1	1	1	2	2	2	2	2	2	2
112	3160.8	1	1	1	1	1	1	1	1	1	1	1	1	1	1	1	2	2	2	2	2	2	2	2	2	2
113	841.2	2	2	2	2	2	2	2	2	2	2	2	2	2	2	2	3	3	3	3	3	3	3	3	3	3
124	753.3	1	1	1	1	1	1	1	1	1	1	1	1	1	1	1	1	1	1	1	1	2	2	2	2	2
126	1693.7	1	1	1	1	1	1	1	1	1	1	1	1	1	3	3	3	3	3	4	4	4	4	4	4	4
127	1939.9	1	1	1	1	1	1	1	1	1	1	1	1	1	1	1	1	1	1	2	2	2	2	2	2	2

Department of Physical Geography and Ecosystem Science

Master Thesis in Geographical Information Science

1. *Anthony Lawther:* The application of GIS-based binary logistic regression for slope failure susceptibility mapping in the Western Grampian Mountains, Scotland (2008).

2. *Rickard Hansen:* Daily mobility in Grenoble Metropolitan Region, France. Applied GIS methods in time geographical research (2008).

3. *Emil Bayramov:* Environmental monitoring of bio-restoration activities using GIS and Remote Sensing (2009).

4. *Rafael Villarreal Pacheco:* Applications of Geographic Information Systems as an analytical and visualization tool for mass real estate valuation: a case study of Fontibon District, Bogota, Columbia (2009).

5. *Siri Oestreich Waage:* a case study of route solving for oversized transport: The use of GIS functionalities in transport of transformers, as part of maintaining a reliable power infrastructure (2010).

6. *Edgar Pimiento:* Shallow landslide susceptibility – Modelling and validation (2010).

7. *Martina Schäfer:* Near real-time mapping of floodwater mosquito breeding sites using aerial photographs (2010).

8. *August Pieter van Waarden-Nagel:* Land use evaluation to assess the outcome of the programme of rehabilitation measures for the river Rhine in the Netherlands (2010).

9. *Samira Muhammad:* Development and implementation of air quality data mart for Ontario, Canada: A case study of air quality in Ontario using OLAP tool. (2010).

10. *Fredros Oketch Okumu*: Using remotely sensed data to explore spatial and temporal relationships between photosynthetic productivity of vegetation and malaria transmission intensities in selected parts of Africa (2011).

11. *Svajunas Plunge:* Advanced decision support methods for solving diffuse water pollution problems (2011).

12. *Jonathan Higgins:* Monitoring urban growth in greater Lagos: A case study using GIS to monitor the urban growth of Lagos 1990 - 2008 and produce future growth prospects for the city (2011).

13. *Mårten Karlberg:* Mobile Map Client API: Design and Implementation for Android (2011).

14. *Jeanette McBride:* Mapping Chicago area urban tree canopy using color infrared imagery (2011).

15. *Andrew Farina:* Exploring the relationship between land surface temperature and vegetation abundance for urban heat island mitigation in Seville, Spain (2011).

16. *David Kanyari*: Nairobi City Journey Planner: An online and a Mobile Application (2011).

17. *Laura V. Drews:* Multi-criteria GIS analysis for siting of small wind power plants - A case study from Berlin (2012).

18. *Qaisar Nadeem:* Best living neighborhood in the city - A GIS based multi criteria evaluation of ArRiyadh City (2012).

19. *Ahmed Mohamed El Saeid Mustafa:* Development of a photo voltaic building rooftop integration analysis tool for GIS for Dokki District, Cairo, Egypt (2012).

20. *Daniel Patrick Taylor*: Eastern Oyster Aquaculture: Estuarine Remediation via Site Suitability and Spatially Explicit Carrying Capacity Modeling in Virginia's Chesapeake Bay (2013).

21. *Angeleta Oveta Wilson:* A Participatory GIS approach to *unearthing* Manchester's Cultural Heritage '*gold mine'* (2013).

22. *Ola Svensson:* Visibility and Tholos Tombs in the Messenian Landscape: A Comparative Case Study of the Pylian Hinterlands and the Soulima Valley (2013).

23. *Monika Ogden:* Land use impact on water quality in two river systems in South Africa (2013).

24. *Stefan Rova:* A GIS based approach assessing phosphorus load impact on Lake Flaten in Salem, Sweden (2013).

25. *Yann Buhot:* Analysis of the history of landscape changes over a period of 200 years. How can we predict past landscape pattern scenario and the impact on habitat diversity? (2013).

26. *Christina Fotiou:* Evaluating habitat suitability and spectral heterogeneity models to predict weed species presence (2014).

27. *Inese Linuza:* Accuracy Assessment in Glacier Change Analysis (2014).

28. *Agnieszka Griffin:* Domestic energy consumption and social living standards: a GIS analysis within the Greater London Authority area (2014).

29. *Brynja Guðmundsdóttir:* Detection of potential arable land with remote sensing and GIS - A Case Study for Kjósarhreppur (2014).

30. *Oleksandr Nekrasov:* Processing of MODIS Vegetation Indices for analysis of agricultural droughts in the southern Ukraine between the years 2000-2012 (2014).

31. *Sarah Tressel:* Recommendations for a polar Earth science portal in the context of Arctic Spatial Data Infrastructure (2014).

32. *Caroline Gevaert:* Combining Hyperspectral UAV and Multispectral Formosat-2 Imagery for Precision Agriculture Applications (2014).

33. *Salem Jamal-Uddeen:* Using GeoTools to implement the multi-criteria evaluation analysis - weighted linear combination model (2014).

34. *Samanah Seyedi-Shandiz:* Schematic representation of geographical railway network at the Swedish Transport Administration (2014).

35. *Kazi Masel Ullah:* Urban Land-use planning using Geographical Information System and analytical hierarchy process: case study Dhaka City (2014).

36. *Alexia Chang-Wailing Spitteler:* Development of a web application based on MCDA and GIS for the decision support of river and floodplain rehabilitation projects (2014).

37. *Alessandro De Martino:* Geographic accessibility analysis and evaluation of potential changes to the public transportation system in the City of Milan (2014).

38. *Alireza Mollasalehi:* GIS Based Modelling for Fuel Reduction Using Controlled Burn in Australia. Case Study: Logan City, QLD (2015).

39. *Negin A. Sanati:* Chronic Kidney Disease Mortality in Costa Rica; Geographical Distribution, Spatial Analysis and Non-traditional Risk Factors (2015).

40. *Karen McIntyre:* Benthic mapping of the Bluefields Bay fish sanctuary, Jamaica (2015).

41. *Kees van Duijvendijk:* Feasibility of a low-cost weather sensor network for agricultural purposes: A preliminary assessment (2015).

42. *Sebastian Andersson Hylander:* Evaluation of cultural ecosystem services using GIS (2015).

43. *Deborah Bowyer:* Measuring Urban Growth, Urban Form and Accessibility as Indicators of Urban Sprawl in Hamilton, New Zealand (2015).

44. *Stefan Arvidsson:* Relationship between tree species composition and phenology extracted from satellite data in Swedish forests (2015).

45. *Damián Giménez Cruz*: GIS-based optimal localisation of beekeeping in rural Kenya (2016).

46. *Alejandra Narváez Vallejo:* Can the introduction of the topographic indices in LPJ-GUESS improve the spatial representation of environmental variables? (2016).

47. *Anna Lundgren:* Development of a method for mapping the highest coastline in Sweden using breaklines extracted from high resolution digital elevation models (2016).

48. *Oluwatomi Esther Adejoro:* Does location also matter? A spatial analysis of social achievements of young South Australians (2016).

49. *Hristo Dobrev Tomov:* Automated temporal NDVI analysis over the Middle East for the period 1982 - 2010 (2016).

50. *Vincent Muller:* Impact of Security Context on Mobile Clinic Activities A GIS Multi Criteria Evaluation based on an MSF Humanitarian Mission in Cameroon (2016).

51. *Gezahagn Negash Seboka:* Spatial Assessment of NDVI as an Indicator of Desertification in Ethiopia using Remote Sensing and GIS (2016).

52. *Holly Buhler:* Evaluation of Interfacility Medical Transport Journey Times in Southeastern British Columbia. (2016).

53. *Lars Ole Grottenberg*: Assessing the ability to share spatial data between emergency management organisations in the High North (2016).

54. *Sean Grant:* The Right Tree in the Right Place: Using GIS to Maximize the Net Benefits from Urban Forests (2016).

55. *Irshad Jamal:* Multi-Criteria GIS Analysis for School Site Selection in Gorno-Badakhshan Autonomous Oblast, Tajikistan (2016).

56. *Fulgencio Sanmartín:* Wisdom-volkano: A novel tool based on open GIS and time-series visualization to analyse and share volcanic data (2016).

57. *Nezha Acil:* Remote sensing-based monitoring of snow cover dynamics and its influence on vegetation growth in the Middle Atlas Mountains (2016).

58. *Julia Hjalmarsson:* A Weighty Issue: Estimation of Fire Size with Geographically Weighted Logistic Regression (2016).

59. *Mathewos Tamiru Amato:* Using multi-criteria evaluation and GIS for chronic food and nutrition insecurity indicators analysis in Ethiopia (2016).

60. *Karim Alaa El Din Mohamed Soliman El Attar:* Bicycling Suitability in Downtown, Cairo, Egypt (2016).

61. *Gilbert Akol Echelai:* Asset Management: Integrating GIS as a Decision Support Tool in Meter Management in National Water and Sewerage Corporation (2016).

62. *Terje Slinning:* Analytic comparison of multibeam echo soundings (2016).

63. *Gréta Hlín Sveinsdóttir:* GIS-based MCDA for decision support: A framework for wind farm siting in Iceland (2017).

64. *Jonas Sjögren:* Consequences of a flood in Kristianstad, Sweden: A GIS-based analysis of impacts on important societal functions (2017).

65. *Nadine Raska:* 3D geologic subsurface modelling within the Mackenzie Plain, Northwest Territories, Canada (2017).

66. *Panagiotis Symeonidis*: Study of spatial and temporal variation of atmospheric optical parameters and their relation with PM 2.5 concentration over Europe using GIS technologies (2017).

67. *Michaela Bobeck:* A GIS-based Multi-Criteria Decision Analysis of Wind Farm Site Suitability in New South Wales, Australia, from a Sustainable Development Perspective (2017).

68. *Raghdaa Eissa*: Developing a GIS Model for the Assessment of Outdoor Recreational Facilities in New Cities Case Study: Tenth of Ramadan City, Egypt (2017).

69. *Zahra Khais Shahid*: Biofuel plantations and isoprene emissions in Svea and Götaland (2017).

70. *Mirza Amir Liaquat Baig*: Using geographical information systems in epidemiology: Mapping and analyzing occurrence of diarrhea in urban - residential area of Islamabad, Pakistan (2017).

71. *Joakim Jörwall*: Quantitative model of Present and Future well-being in the EU-28: A spatial Multi-Criteria Evaluation of socioeconomic and climatic comfort factors (2017).

72. *Elin Haettner*: Energy Poverty in the Dublin Region: Modelling Geographies of Risk (2017).

73. *Harry Eriksson*: Geochemistry of stream plants and its statistical relations to soil- and bedrock geology, slope directions and till geochemistry. A GIS-analysis of small catchments in northern Sweden (2017).

74. *Daniel Gardevärn:* PPGIS and Public meetings – An evaluation of public participation methods for urban planning (2017).

75. *Kim Friberg:* Sensitivity Analysis and Calibration of Multi Energy Balance Land Surface Model Parameters (2017).

76. *Viktor Svanerud:* Taking the bus to the park? A study of accessibility to green areas in Gothenburg through different modes of transport (2017).

77. *Lisa-Gaye Greene*: Deadly Designs: The Impact of Road Design on Road Crash Patterns along Jamaica's North Coast Highway (2017).

78. *Katarina Jemec Parker*: Spatial and temporal analysis of fecal indicator bacteria concentrations in beach water in San Diego, California (2017).

79. *Angela Kabiru*: An Exploratory Study of Middle Stone Age and Later Stone Age Site Locations in Kenya's Central Rift Valley Using Landscape Analysis: A GIS Approach (2017).

80. *Kristean Björkmann*: Subjective Well-Being and Environment: A GIS-Based Analysis (2018).

81. *Williams Erhunmonmen Ojo*: Measuring spatial accessibility to healthcare for people living with HIV-AIDS in southern Nigeria (2018).

82. *Daniel Assefa*: Developing Data Extraction and Dynamic Data Visualization (Styling) Modules for Web GIS Risk Assessment System (WGRAS). (2018).

83. *Adela Nistora*: Inundation scenarios in a changing climate: assessing potential impacts of sea-level rise on the coast of South-East England (2018).

84. *Marc Seliger*: Thirsty landscapes - Investigating growing irrigation water consumption and potential conservation measures within Utah's largest master-planned community: Daybreak (2018).

85. *Luka Jovičić*: Spatial Data Harmonisation in Regional Context in Accordance with INSPIRE Implementing Rules (2018).

86. *Christina Kourdounouli*: Analysis of Urban Ecosystem Condition Indicators for the Large Urban Zones and City Cores in EU (2018).

87. *Jeremy Azzopardi*: Effect of distance measures and feature representations on distance-based accessibility measures (2018).

88. *Patrick Kabatha*: An open source web GIS tool for analysis and visualization of elephant GPS telemetry data, alongside environmental and anthropogenic variables (2018).

89. *Richard Alphonce Giliba*: Effects of Climate Change on Potential Geographical Distribution of Prunus africana (African cherry) in the Eastern Arc Mountain Forests of Tanzania (2018).

90. *Eiður Kristinn Eiðsson*: Transformation and linking of authoritative multi-scale geodata for the Semantic Web: A case study of Swedish national building data sets (2018).

91. *Niamh Harty*: HOP!: a PGIS and citizen science approach to monitoring the condition of upland paths (2018).

92. *José Estuardo Jara Alvear*: Solar photovoltaic potential to complement hydropower in Ecuador: A GIS-based framework of analysis (2018).

93. *Brendan O'Neill*: Multicriteria Site Suitability for Algal Biofuel Production Facilities (2018).

94. *Roman Spataru*: Spatial-temporal GIS analysis in public health – a case study of polio disease (2018).

95. *Alicja Miodońska*: Assessing evolution of ice caps in Suðurland, Iceland, in years 1986 - 2014, using multispectral satellite imagery (2019).

96. *Dennis Lindell Schettini*: A Spatial Analysis of Homicide Crime's Distribution and Association with Deprivation in Stockholm Between 2010-2017 (2019).

97. *Damiano Vesentini*: The Po Delta Biosphere Reserve: Management challenges and priorities deriving from anthropogenic pressure and sea level rise (2019).

98. *Emilie Arnesten*: Impacts of future sea level rise and high water on roads, railways and environmental objects: a GIS analysis of the potential effects of increasing sea levels and highest projected high water in Scania, Sweden (2019).

99. *Syed Muhammad Amir Raza*: Comparison of geospatial support in RDF stores: Evaluation for ICOS Carbon Portal metadata (2019).

100. *Hemin Tofiq*: Investigating the accuracy of Digital Elevation Models from UAV images in areas with low contrast: A sandy beach as a case study (2019).

101. *Evangelos Vafeiadis*: Exploring the distribution of accessibility by public transport using spatial analysis. A case study for retail concentrations and public hospitals in Athens (2019).

102. *Milan Sekulic*: Multi-Criteria GIS modelling for optimal alignment of roadway by-passes in the Tlokweng Planning Area, Botswana (2019).

103. *Ingrid Piirisaar*: A multi-criteria GIS analysis for siting of utility-scale photovoltaic solar plants in county Kilkenny, Ireland (2019).

104. *Nigel Fox*: Plant phenology and climate change: possible effect on the onset of various wild plant species' first flowering day in the UK (2019).

105. *Gunnar Hesch*: Linking conflict events and cropland development in Afghanistan, 2001 to 2011, using MODIS land cover data and Uppsala Conflict Data Programme (2019).

106. *Elijah Njoku*: Analysis of spatial-temporal pattern of Land Surface Temperature (LST) due to NDVI and elevation in Ilorin, Nigeria (2019).

107. *Katalin Bunyevácz*: Development of a GIS methodology to evaluate informal urban green areas for inclusion in a community governance program (2019).

108. *Paul dos Santos*: Automating synthetic trip data generation for an agent-based simulation of urban mobility (2019).

109. *Robert O' Dwyer*: Land cover changes in Southern Sweden from the mid-Holocene to present day: Insights for ecosystem service assessments (2019).

110. *Daniel Klingmyr*: Global scale patterns and trends in tropospheric NO2 concentrations (2019).

111. *Marwa Farouk Elkabbany*: Sea Level Rise Vulnerability Assessment for Abu Dhabi, United Arab Emirates (2019).

112. *Jip Jan van Zoonen*: Aspects of Error Quantification and Evaluation in Digital Elevation Models for Glacier Surfaces (2020).

113. *Georgios Efthymiou*: The use of bicycles in a mid-sized city – benefits and obstacles identified using a questionnaire and GIS (2020).

114. *Haruna Olayiwola Jimoh*: Assessment of Urban Sprawl in MOWE/IBAFO Axis of Ogun State using GIS Capabilities (2020).

115. *Nikolaos Barmpas Zachariadis*: Development of an iOS, Augmented Reality for disaster management (2020).

116. *Ida Storm*: ICOS Atmospheric Stations: Spatial Characterization of CO2 Footprint Areas and Evaluating the Uncertainties of Modelled CO2 Concentrations (2020).

117. *Alon Zuta*: Evaluation of water stress mapping methods in vineyards using airborne thermal imaging (2020).

118. *Marcus Eriksson*: Evaluating structural landscape development in the municipality Upplands-Bro, using landscape metrics indices (2020).

119. *Ane Rahbek Vierø*: Connectivity for Cyclists? A Network Analysis of Copenhagen's Bike Lanes (2020).

120. *Cecilia Baggini*: Changes in habitat suitability for three declining Anatidae species in saltmarshes on the Mersey estuary, North-West England (2020).

121. *Bakrad Balabanian*: Transportation and Its Effect on Student Performance (2020).

122. *Ali Al Farid*: Knowledge and Data Driven Approaches for Hydrocarbon Microseepage Characterizations: An Application of Satellite Remote Sensing (2020).

123. *Bartlomiej Kolodziejczyk*: Distribution Modelling of Gene Drive-Modified Mosquitoes and Their Effects on Wild Populations (2020).

124. *Alexis Cazorla*: Decreasing organic nitrogen concentrations in European water bodies - links to organic carbon trends and land cover (2020).

125. *Kharid Mwakoba*: Remote sensing analysis of land cover/use conditions of community-based wildlife conservation areas in Tanzania (2021).

126. *Chinatsu Endo*: Remote Sensing Based Pre-Season Yellow Rust Early Warning in Oromia, Ethiopia (2021).

127. *Berit Mohr*: Using remote sensing and land abandonment as a proxy for long-term human out-migration. A Case Study: Al-Hassakeh Governorate, Syria (2021).

128. *Kanchana Nirmali Bandaranayake*: Considering future precipitation in delineation locations for water storage systems - Case study Sri Lanka (2021).

129. *Emma Bylund*: Dynamics of net primary production and food availability in the aftermath of the 2004 and 2007 desert locust outbreaks in Niger and Yemen (2021).

130. *Shawn Pace*: Urban infrastructure inundation risk from permanent sea-level rise scenarios in London (UK), Bangkok (Thailand) and Mumbai (India): A comparative analysis (2021).

131. *Oskar Evert Johansson*: The hydrodynamic impacts of Estuarine Oyster reefs, and the application of drone technology to this study (2021).

132. *Pritam Kumarsingh*: A Case Study to develop and test GIS/SDSS methods to assess the production capacity of a Cocoa Site in Trinidad and Tobago (2021).

133. *Muhammad Imran Khan*: Property Tax Mapping and Assessment using GIS (2021).

134. *Domna Kanari*: Mining geosocial data from Flickr to explore tourism patterns: The case study of Athens (2021).

135. *Mona Tykesson Klubien*: Livestock-MRSA in Danish pig farms (2021).

136. *Ove Njøten*: Comparing radar satellites. Use of Sentinel-1 leads to an increase in oil spill alerts in Norwegian waters (2021).

137. *Panagiotis Patrinos*: Change of heating fuel consumption patterns produced by the economic crisis in Greece (2021).

138. *Lukasz Langowski*: Assessing the suitability of using Sentinel-1A SAR multi-temporal imagery to detect fallow periods between rice crops (2021).

139. *Jonas Tillman*: Perception accuracy and user acceptance of legend designs for opacity data mapping in GIS (2022).

140. *Gabriela Olekszyk*: ALS (Airborne LIDAR) accuracy: Can potential low data quality of ground points be modelled/detected? Case study of 2016 LIDAR capture over Auckland, New Zealand (2022).

141. *Luke Aspland*: Weights of Evidence Predictive Modelling in Archaeology (2022).

142. *Luís Fareleira Gomes*: The influence of climate, population density, tree species and land cover on fire pattern in mainland Portugal (2022).

143. *Andreas Eriksson*: Mapping Fire Salamander (Salamandra salamandra) Habitat Suitability in Baden-Württemberg with Multi-Temporal Sentinel-1 and Sentinel-2 Imagery (2022).

144. *Lisbet Hougaard Baklid*: Geographical expansion rate of a brown bear population in Fennoscandia and the factors explaining the directional variations (2022).

145. *Victoria Persson*: Mussels in deep water with climate change: Spatial distribution of mussel (Mytilus galloprovincialis) growth offshore in the French Mediterranean with respect to climate change scenario RCP 8.5 Long Term and Integrated Multi-Trophic Aquaculture (IMTA) using Dynamic Energy Budget (DEB) modelling (2022).

146. *Benjamin Bernard Fabien Gérard Borgeais*: Implementing a multi-criteria GIS analysis and predictive modelling to locate Upper Palaeolithic decorated caves in the Périgord noir, France (2022).

147. *Bernat Dorado-Guerrero*: Assessing the impact of post-fire restoration interventions using spectral vegetation indices: A case study in El Bruc, Spain (2022).

148. *Ignatius Gabriel Aloysius Maria Perera*: The Influence of Natural Radon Occurrence on the Severity of the COVID-19 Pandemic in Germany: A Spatial Analysis (2022).

149. *Mark Overton*: An Analysis of Spatially-enabled Mobile Decision Support Systems in a Collaborative Decision-Making Environment (2022).

150. *Viggo Lunde*: Analysing methods for visualizing time-series datasets in open-source web mapping (2022).

151. *Johan Viscarra Hansson*: Distribution Analysis of Impatiens glandulifera in Kronoberg County and a Pest Risk Map for Alvesta Municipality (2022).

152. *Vincenzo Poppiti*: GIS and Tourism: Developing strategies for new touristic flows after the Covid-19 pandemic (2022).

153. *Henrik Hagelin*: Wildfire growth modelling in Sweden - A suitability assessment of available data (2023).

154. *Gabriel Romeo Ferriols Pavico*: Where there is road, there is fire (influence): An exploratory study on the influence of roads in the spatial patterns of Swedish wildfires of 2018 (2023).

155. *Colin Robert Potter*: Using a GIS to enable an economic, land use and energy output comparison between small wind powered turbines and large-scale wind farms: the case of Oslo, Norway (2023).

156. *Krystyna Muszel*: Impact of Sea Surface Temperature and Salinity on Phytoplankton blooms phenology in the North Sea (2023).

157. *Tobias Rydlinge*: Urban tree canopy mapping - an open source deep learning approach (2023).

158. *Albert Wellendorf*: Multi-scale Bark Beetle Predictions Using Machine Learning (2023).

159. *Manolis Papadakis*: Use of Satellite Remote Sensing for Detecting Archaeological Features: An Example from Ancient Corinth, Greece (2023).

160. *Konstantinos Sourlamtas*: Developing a Geographical Information System for a water and sewer network, for monitoring, identification and leak repair - Case study: Municipal Water Company of Naoussa, Greece (2023).

161. *Xiaoming Wang*: Identification of restoration hotspots in landscape-scale green infrastructure planning based on model-predicted connectivity forest (2023).

162. *Sarah Sienaert*: Usability of Sentinel-1 C-band VV and VH SAR data for the detection of flooded oil palm (2023).

163. *Katarina Ekeroot*: Uncovering the spatial relationships between Covid-19 vaccine coverage and local politics in Sweden (2023).

164. *Nikolaos Kouskoulis*: Exploring patterns in risk factors for bark beetle attack during outbreaks triggered by drought stress with harvester data on attacked trees: A case study in Southeastern Sweden (2023).

165. *Jonas Almén*: Geographic polarization and clustering of partisan voting: A local-level analysis of Stockholm Municipality (2023).

166. *Sara Sharon Jones*: Tree species impact on Forest Fire Spread Susceptibility in Sweden (2023).

167. *Takura Matswetu*: Towards a Geographic Information Systems and Data-Driven Integration Management. Studying holistic integration through spatial accessibility of services in Tampere, Finland. (2023).

168. *Duncan Jones*: Investigating the influence of the tidal regime on harbour porpoise *Phocoena phocoena* distribution in Mount's Bay, Cornwall (2023).

169. *Jason Craig Joubert*: A comparison of remote sensed semi-arid grassland vegetation anomalies detected using MODIS and Sentinel-3, with anomalies in ground-based eddy covariance flux measurements (2023).

170. *Anastasia Sarelli*: Land cover classification using machine-learning techniques applied to fused multi-modal satellite imagery and time series data (2024).

171. *Athanasios Senteles*: Integrating Local Knowledge into the Spatial Analysis of Wind Power: The case study of Northern Tzoumerka, Greece (2024).

172. *Rebecca Borg:* Using GIS and satellite data to assess access of green area for children living in growing cities (2024).

173. *Panagiotis–Dimitrios Tsachageas*: Multicriteria Evaluation in Real Estate Land-use Suitability Analysis: The case of Volos, Greece (2024).

174. *Hugo Nilsson*: Inferring lane-level topology of signalised intersections from aerial imagery and OpenStreetMap using deep learning (2024).

175. *Pavlos Alexantonakis*: Estimating lake water volume fluctuations using Sentinel-2 and ICESat-2 remote sensing data (2024).

176. *Karl-Martin Wigen*: Physical barriers and where to find them (2024).

177. *Martin Storsnes*: Temporal RX-algorithm performance on Sentinel-2 images (2024).

178. *Saulė Gabrielė Petraitytė*: The Relation Between Covid-19 Vaccination and Voting Trends in Lithuania: A Spatial Analysis (2024).

179. *Pedro Martinez Duran*: Olive yield forecasting from remote sensing and climate datasets in the Jaen province (Spain) (2024).

180. *Josefine Kynde Hämberg*: Proximity to Urban Green Spaces for Older Adults in Specific Housings - a Case Study of Malmö, Sweden (2024).

181. *Max Bengtsson*: A Site Selection of An Energy Island in the North Sea: Optimal Location in an Ecological and an Economic Scenario Using a Multicriteria Decision Analysis (MCDA) (2024).

182. *Anna Börmann*: Assessing Great Britain as a relocation site for the threatened Iberian Lynx in a changing climate (2024).

183. *Josephine Roosli*: Flood Risk Assessment for the Kävlinge River for Present and Future Climate Scenarios using HEC-RAS Rain-on-Grid (2024).

184. *Seán Flanagan*: Spatiotemporal dynamics of E-scooter sharing ridership and their associations with the built environment: A Swedish comparative study (2024).

185. *Wouter Vorsters*: Assessing the Impact of Combined Sewer Overflow on the Habitat of Lampetra planeri: A Case Study in Flanders, Belgium (2025).

186. *Kathleen Macdonald*: Cetacean strandings on the Scottish coast: coastal accessibility factors lead to underreporting (2025).

187. *Athanasios Emmanouil Mourampetzis*: Navigating the Shadows: A Comparative Analysis of SAR and Optical Imagery for Detecting (Dark) Vessels (2025).

188. *Nizam-ud-Din*: Spatial Land Records System using Geospatial Techniques: a case study of a Mid-Sized Village in Pakistan (2025).

189. *Nedim Nasic Kjellgren*: Linked Geodata: Improving Rooftop Photovoltaic Production Estimates through BIM-GIS Integration using Semantic Web Technologies (2025).

190. *Vedrana Pretkovic*: Spatio-temporal vegetation changes in the Pacific-Chocó region of Colombia during the conflict and post-conflict periods (2025).

191. *Evelina Bengtsson*: A Socioeconomic Dimension of Crime: A Spatial Study of Firearm-related Violence in Malmö (2025).

192. *Martynas Bielinis*: Application of C-band Radar Interferometry for Dune Monitoring in the Curonian Spit (2025).

193. *Paulina Magdalena Rieke*: Case study of the benefits of BIM and GIS solutions used on a live infrastructure project (2025).

194. *Alina Schärer*: Evaluating the Impact of Urban Green Spaces and Vegetation Characteristics on Land Surface Temperature Across Swiss Cities Using Machine Learning (2025).

195. *Paul Stewart:* Where is wild in Glasgow's Southside? A test of the applicability of relative wildness mapping to suburban Scotland (2025).

196. *Georgios Fylakis:* Spatiotemporal analysis of the integration between shared e-scooters and public transport: Case studies in Oslo and Stockholm (2025).

197. *Andreas Klasson*: Generating 3D building models according to Swedish building specification using footprints and airborne laser scanning (2025).

198. *Agaton Järemo Lawin*: The spread of Japanese knotweed in Scania: Invasion suitability prediction using species distribution modelling (2025).

199. *Jesse Stewart:* Contextualizing the Geographic Influence on Infantry Manoeuvrability in a Historical Battlefield Using GIS: A Case Study of the Canadian Corps in the Second Battle of Passchendaele, First World War (2025).

200. *Oskar Vejkdal Thorsberg*: Automatic geometry extraction in digital building permits: A case study using BIM and NS Building (2025).

201. *Spyridon Gerafentis*: Impact of the COVID-19 "Lockdown" on Air Quality in Athens (2025).

202. *Symeon Andriotis*: Political Violence in Athens, Greece (2008-2024): A Machine Learning Approach for Predictive Modelling of Spatial Risk Patterns (2025).

203. *Simon Westman*: Detecting Structurally Old Scots Pine: A Crown-Metric Approach Using National ALS and LIFT Enrichment (2026).

204. *Freja Randeris Kristoffersen*: Satellite-Derived Bathymetry of Danish Coastal Waters Using Machine Learning with Sentinel-2 and ICESat-2 data (2026).

205. *Markus Honkanen*: Securitas Per Scientiam: GIS-MCDA of Civil Defence Shelter Distribution Efficiency in the Helsinki Capital Region (2026).

206. *Amanda Carolina Santos Motta*: Visualization Tools for Simulation Results Based on 3D City Models: An Urban Planner-Focused Study (2026).

207. *Gintars Krumins*: Mapping forest felling activities in Latvia from Sentinel-2 satellite imagery using machine learning (2026).

208. *Jenny Berntsson*: Using Multi-criteria GIS analysis in nature conservation planning in Lilla Edet municipality (2026).

209. *Sebastian Daland*: Flood impacts on road accessibility and buildings in Gothenburg during a 100-year rainfall event (2026).

210. *Polyxeni Karapanagiotidou*: GIS-based Multi-Criteria Decision Analysis (MCDA) framework for Flood Risk Assessment in the Thermi Basin (2026).

211. *Nour Abdulmagid A. Bensaid*: Urban Expansion and its Relation to the Urban Heat Island Effect: A Case Study of Tripoli, Libya (2026).

212. *Iris Krohn*: Compound Extreme Events in Hamburg, Germany: A Flood Risk Assessment (2026).

213. *Johan Wahlberg*: Towards Data-Centric Geospatial Applications: A Knowledge Graph Approach to Road Maintenance in Stockholm, Sweden (2026).

214. *Athanasios Fyntanidis*: Towards Data-Centric Geospatial Applications: Machine Learning–Driven Assessment of Urban Heat Island Intensity in Athens: Integrating Remote Sensing, Landscape Metrics, and Green Infrastructure for Climate-Resilient Urban Planning (2026).

215. *J.C.W. van Diest*: Detecting Spatial Impacts of Violence through Remote Sensing: A Case Study of Conflict-Affected Regions in Central Mali (2026).

216. *Ingrid Martha Kintu*: Monitoring Landslide Disturbance and Forest Recovery in Afromontane Landscapes: The Case of Nyungwe Forest Reserve, Rwanda (2026).